Received: 13 June 2023 | Revised: 27 October 2023 | Accepted: 17 December 2023

DOI: 10.33012/navi.637

ORIGINAL ARTICLE

Geodetic Altitude from Barometer and Weather Data for GNSS Integrity Monitoring in Aviation

Maximilian Simonetti | **Omar García Crespillo**

Institute of Communications and Navigation, German Aerospace Center (DLR), Oberpfaffenhofen-Wessling, Germany

Abstract

Vertical navigation is crucial for safe aircraft separation and has been traditionally based on the pressure altitude provided by barometric altimeters. New aviation operations require robust determination of geodetic altitude and are expected to primarily rely on a global navigation satellite system (GNSS). Because deviations between pressure and geodetic altitudes can reach hundreds of meters, an altitude harmonization is needed to use barometers in combination with GNSS. In this paper, we first present a methodology to compute an accurate geodetic altitude from barometer and external weather data. Secondly, we derive error and threat models of this geodetic altitude. Finally, we employ these models within a GNSS integrity monitoring algorithm augmented with the derived altitude. We assess our methodologies against flight test measurements and availability simulations of localizer performance with vertical guidance operations. These analyses illustrate the potential benefits of employing barometers as augmentation or stand-alone systems for geodetic altitude navigation.

Keywords

ABAS, ARAIM, ERA5, integrated navigation, LPV-200, pressure altitude, vertical navigation

1 | INTRODUCTION

Vertical navigation is crucial for safe air traffic management (ATM); in particular, it is fundamental for aircraft vertical separation. Vertical navigation is traditionally ensured by the definition of flight levels (FLs), which are surfaces of constant *QNE* pressure altitude. Pressure (or barometric) altitude in aviation is computed from pressure measurements performed by barometers within airborne air data systems (ADSs). The derivation of this altitude information is based on the international standard atmosphere (ISA) model. The pressure altitude (typically measured in feet) between the aircraft pressure surface and the ISA standard mean sea level (MSL) pressure level is the QNE pressure altitude.

Altitude is a vertical distance between a point and a certain reference surface, along the normal line to this surface. The altitude increment with respect to distance is defined by the adopted altitude scale. An altitude that would be read on an hypothetical ruler is a geometric altitude, i.e., its scale is geometric. In contrast, pressure altitude has a geopotential scale. Geodetic altitude is the geometric altitude

above a reference ellipsoid of the Earth, e.g., the World Geodetic System (WGS) 84 ellipsoid, which is used within global navigation satellite systems (GNSSs). The QNE pressure altitude can deviate by up to hundreds of meters from the true geodetic altitude because of differences in altitude references and scales as well as the deviation of the ISA model from reality. QNE pressure altitudes of points at the same geodetic altitude can differ from each other and over time depending on the atmospheric pressure values at those points. Therefore, this altitude can be regarded as a virtual altitude. Airplanes flying in the same region at the same time can rely on the QNE pressure altitude to ensure vertical separation between them because their altitude data are the same. Pressure altitude is also traditionally employed in aviation within third-order control loops to damp the inherent instability of the vertical channel of inertial navigation systems (INSs) (Groves, 2013; Radio Technical Commission for Aeronautics [RTCA], 2020; Siouris, 1993).

In aviation, reliable information about safe separation from the ground is also needed, as is the case below the so-called transition altitudes (e.g., 18000 ft in the United States). This information is traditionally obtained from barometers by setting a reference isobar as the isobar at the airport's location (*QFE* approach) or an estimate of the actual MSL isobar (*QNH* approach) at the same horizontal location of the airport (International Civil Aviation Organization [ICAO], 2016; RTCA, 2020).

The pressure altitude overestimates the true geopotential altitude above a certain reference when the atmospheric temperature at that reference is lower than predicted by the ISA. This overestimate is safety-critical, as it leads the pilot to overestimate the altitude above that reference, which could be the ground surface in the QFE case (ICAO, 2018c; RTCA, 2020). Minimum safe altitudes (MSAs) are threshold altitudes below which it is not safe to fly because of the presence of terrain or other obstacles (ICAO, 2018c). ICAO (2018d) provides different methods for adjusting the MSA for the case in which the surface ambient temperature largely differs from its ISA-expected value. Some of these methods are based on the processing of temperature measurements broadcast by airports or ground stations. Therefore, their effectiveness is inversely proportional to the airplane's distance to the airport. In a similar way, as the distance to the airport increases, QNH- or QFE-corrected pressure altitudes can also deviate from the actual geopotential altitude above MSL (AMSL) or above the airport, respectively. Furthermore, it is expected that both the QNH and QFE corrections degrade with time because they are based on half-hourly or hourly weather reports transmitted by airports (ICAO, 2016, 2018b). Moreover, the transmitted pressure values used for QNH or QFE corrections are rounded down to the nearest lower whole hectopascal (ICAO, 2018b). Thus, the maximum rounding error of their corresponding actual pressures may be 99 Pa. Under ISA MSL conditions, this translates to a pressure altitude offset of more than 8 m. Consequently, it can be expected that these corrected barometric altitudes will also deviate in general from the actual geodetic altitude, even after their references are shifted to the chosen Earth ellipsoid and their altitude scale is converted from geopotential to geometric. One approach to obtain the geometric altitude above MSL and to account for non-standard atmospheric temperature is based on the use of both pressure and temperature measurements within an iterative algorithm, known as the Blanchard algorithm (Blanchard, 1971, 1972; Li & Chueh, 2010; RTCA, 2020). However, in this case, the resulting geometric altitude still presents non-negligible errors, which increase over time.

Highly accurate geodetic altitude information is fundamental for various applications. First, it is essential for critical aviation operations such as precision approaches and automatic landing (ICAO, 2013), which are expected to predominantly rely on GNSS. Furthermore, new urban air mobility (UAM) applications

operate close to the ground and are expected to require robust geodetic altitude information (Aviation Cooperation and Strategies Division [ACS], 2018; Concept of Operations for European UTM Systems consortium [CORUS], 2019; Single European Sky ATM Research Programme Joint Undertaking [SESAR], 2020) for guidance, navigation, and collision avoidance (Torens et al., 2021). The provision of geodetic altitude information in aviation and UAM can also ease the transition of air vehicles between different air spaces (see Figure 1). Finally, it has been shown that accurate geodetic altitude information is fundamental for the convergence of alternative positioning, navigation, and timing (APNT) algorithms based on terrestrial ranging signals (Nossek et al., 2014; Zampieri et al., 2020).

GNSSs provide vertical navigation based on geodetic altitude. However, it is challenging to meet tight vertical requirements via satellite navigation alone, because of inherent GNSS geometrical limitations (Reid et al., 2016) and the potential risk of external interference (Osechas et al., 2022). Augmenting a GNSS with onboard systems can help increase accuracy and safety. Augmentation with onboard systems falls under the definition of aircraft-based augmentation systems (ABASs). The advantage of this type of augmentation is that these systems do not rely on external infrastructures, in contrast to ground-based augmentation systems (GBASs) or satellite-based augmentation systems (SBASs). Indeed, GBASs and SBASs rely on GNSS corrections transmitted from ground stations or geostationary satellites, respectively. Therefore, ABASs can extend accurate navigation services to regions not covered by a GBAS or SBAS.

Current ABAS developments focus on proving that advanced receiver autonomous integrity monitoring (ARAIM) can safely support horizontal and vertical navigation services, thanks to the use of multi-frequency multi-constellation GNSSs. Although ARAIM can ensure high levels of navigation integrity, the attainable protection levels (PLs) are limited by the overbounding of error distributions to account for worst-case expected performance. ARAIM can be considered an ABAS because it extends classic GNSS-based navigation algorithms with additional onboard processing. Nevertheless, ARAIM does not include measurements from other navigation systems. For this reason, ARAIM may still partially suffer from typical GNSS limitations. The availability and continuity of the navigation service may be put at risk by the presence of cycle slips or by reception interruptions of satellite signals during aircraft banking within the maneuvers required for terminal vicinity operations (Garcia Crespillo, 2022). The use of additional onboard sensors such as barometric or radar altimeters can aid GNSS-based navigation to meet the vertical

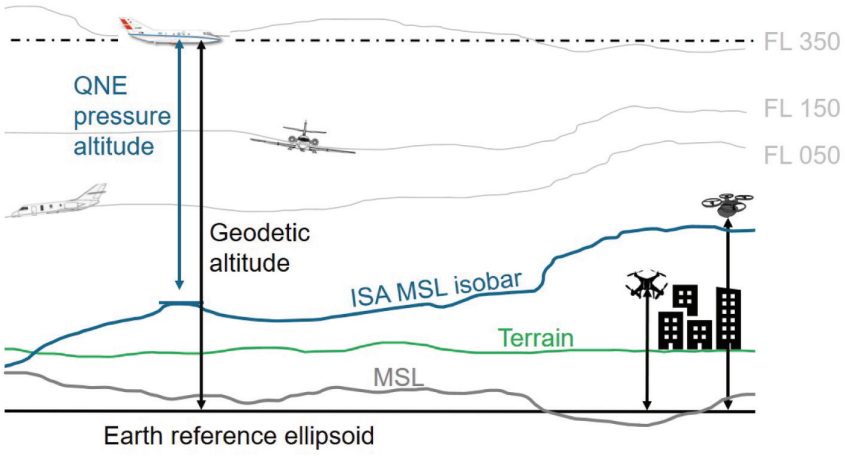

FIGURE 1 FLs, QNE pressure altitude, and various altitude references on a geometric scale

navigation requirements of current and future safety-critical operations. Radar sensors have been used for altitude determination, particularly during take-off and landing, where the terrain is typically flat and aircraft perform minor banking maneuvers (Shively & Hsiao, 2005; Videmsek et al., 2019). However, radar altimetry presents several limitations. Accurate digital terrain elevation data (DTED) are required to obtain the geodetic altitude. Yet, sharp terrain elevation variations may not be observable with available DTED. Moreover, measurement errors increase with increasing altitude above ground.

Barometric altimeters can be used during all flight phases. However, the combination of barometers with (ARAIM) GNSS for vertical navigation with enhanced accuracy and integrity presents different challenges and requires a consideration of the following aspects:

1. the use of external, reliable, and densely available weather data for the definition of accurate reference isobars,
2. a thorough conversion of corrected pressure altitude to geodetic altitude,
3. error models of the resulting geodetic altitude, and
4. dedicated failure analyses, needed for integrity monitoring.

Previous work concerning the conversion of barometric pressure to altitude and/or the augmentation of GNSS-based systems with barometers can be found in the literature. The conversion from QNE pressure to geodetic altitude described by Gaglione et al. (2015) did not feature the altitude scale conversion from geopotential to geometric. A project funded by the European Union has proposed a service for converting QNE or QNH pressure altitudes to geometric altitudes (SESAR, 2022). However, the approach adopted for correcting pressure altitudes makes limited use of weather measurements, and the conversion to geometric altitudes does not include the altitude scale conversion (SESAR, 2021). Similarly, S. Jan et al. (2008) and Lee et al. (2016) corrected the pressure altitude by using (limited) external weather data and neglected the scale conversion when translating the corrected pressure altitude to geodetic altitude. Xu et al. (2021) did not mention any correction or conversion from barometric pressure to geodetic altitude. Ultimately, in none of the aforementioned previous works has the pressure altitude been both corrected with external weather data and rigorously converted to geodetic altitude. Moreover, the analyses of the aforementioned studies were based on flight simulations or on measurements performed at constant locations or on ground vehicles. Thus, these analyses did not allow a proper assessment of the effects on actual pressure measurements concurrently caused by flight dynamics, altitude transitions, and weather phenomena such as wind. In the aforementioned previous works, with the exception of SESAR (2022), barometric altitude measurements were integrated in positioning algorithms based on GNSS. However, the GNSS considered in these previous works was limited to the Global Positioning System (GPS). The integrations were based on weighted least-square (WLS) algorithms, whereby Gaglione et al. (2015) additionally proposed a second architecture based on an integration with GPS (non-advanced) RAIM within an extended Kalman filter (KF). Finally, RTCA (2020) suggested error modeling methodologies for the KF-based integration of barometric altimeters with GNSS/INS.

In this work, we first derive an accurate geodetic altitude from real aircraft barometric pressure measurements coupled with global weather data. Secondly, we augment GNSS WLS ARAIM with this geodetic altitude, which we call the *barometric geodetic altitude*. This paper is structured as follows. Section 2 describes various concepts related to altitude that are relevant for the conversion of pressure

to geodetic altitude. This conversion methodology is then covered in Section 3, which also describes the proposed approach of correcting pressure altitude with external weather data. Section 4 describes the evaluation, with real flight data, of the pressure altitude correction and conversion and then focuses on the derivation of error and threat models of the barometric geodetic altitude. Section 5 extends the baseline ARAIM algorithm to include barometric geodetic altitude measurements and presents the results of applying this navigation integrity architecture to worldwide simulations as well as a real flight. Section 6 provides closing remarks and plans for future work.

2 | ALTITUDE DEFINITIONS

2.1 | Altitude Scales and References

Table 1 shows different altitude definitions according to several possible reference surfaces and altitude scales. In this work, we consider the WGS84 ellipsoid as the reference for the target geodetic altitude h, as it is currently the most widely used reference in navigation. A second possible reference surface is the Geoid, which is a model of the Earth's surface defined as the equipotential surface of the Earth's gravitational field, which best fits, in a least-squares sense, the global MSL (Amin et al., 2019). This is the level of the oceans averaged over the tide cycle. Because water tends to maintain a constant potential energy, it is expected that the Geoid coincides with the MSL, with a difference that is generally less than 1 m worldwide (Groves, 2013).

The geometric altitude of a point above the Geoid is typically called the *orthometric altitude*, herein denoted by H. This term is related to the geodetic altitude as follows:

$$H \approx h - N(L, \lambda) \tag{1}$$

where the Geoid undulation N is the distance of the Geoid from the ellipsoidal surface for a given longitude λ and latitude L (see Figure 2(a)). The Geoid undulation is positive when the Geoid surface is outside the ellipsoid, and it ranges worldwide between approximately −105 and 85 m, as shown in Figure 2(c), according to the Earth gravitational model (EGM) 96 (Lemoine et al., 1998). In this work, we employ EGM96 instead of the more recent and accurate EGM2008, because the former is employed by the weather data provider considered in this work.

TABLE 1
Altitude Definition Grid

	SCALE	
REFERENCE	**Geometric**	**Geopotential**
WGS84 Ellipsoid	Geodetic Altitude, h	Z_g^{wgs84}
MSL	Orthometric Altitude, H	Geopotential Altitude AMSL Z_g^{msl}
ISA MSL		QNE Pressure Altitude, Z_p^{qne}
Airport Isobar		QFE Pressure Altitude, Z_p^{qfe}
Airport Isobar Projected to MSL		QNH Pressure Altitude, Z_p^{qnh}

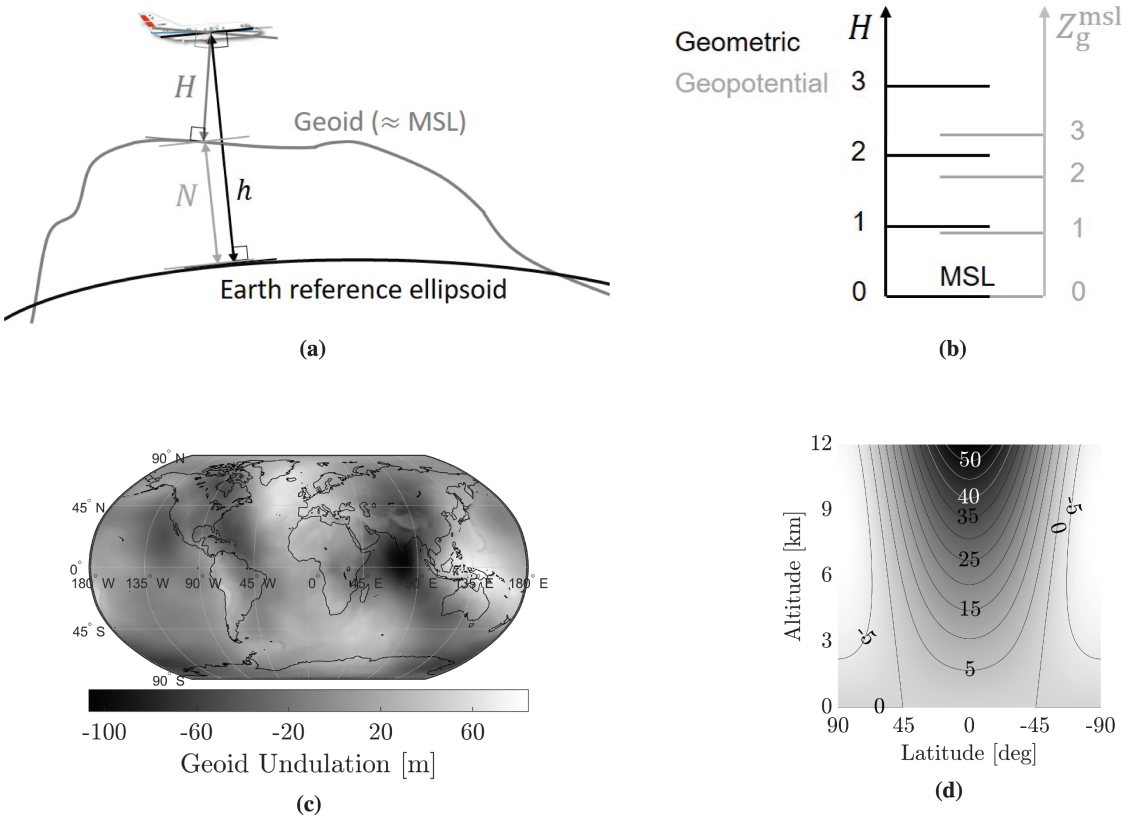

FIGURE 2 Qualitative (top row) and quantitative (bottom row) differences within diverse altitude references (left column) and altitude scales (right column) (a) Relationship between geodetic and orthometric altitudes (b) Altitude scale deviations at the equator, as an example (c) EGM96 Geoid undulations (d) Deviations in meters between geometric and geopotential scales

The geodetic and orthometric altitudes are both geometric altitudes, because of their geometric scale. In contrast, the pressure altitude is a geopotential altitude above a certain isobar surface. The next paragraphs define different types of geopotential altitudes that are relevant within this work. The geopotential altitude AMSL is defined as follows (ICAO, 1993):

$$Z_g^{msl}(L,\lambda,H) := \frac{1}{g_0}\int_0^H g(L,\lambda,z)\mathrm{d}z \tag{2}$$

where $g_0 = 9.80665\ \mathrm{ms}^{-2}$ is the standard acceleration due to gravity at the surface of the Earth.

To solve Equation (2), a geopotential altitude with respect to the WGS84 ellipsoid can be defined as follows (Scherllin-Pirscher et al., 2017):

$$Z_g^{wgs84}(L,\lambda,h) := \frac{1}{g_0}\int_0^h \gamma_h(L,\lambda,z)\mathrm{d}z \tag{3}$$

where γ_h denotes the gravity for a given latitude, longitude, and geodetic altitude. An approximated closed-form, longitude-independent solution of Equation (3) can be given as follows (Scherllin-Pirscher et al., 2017):

$$Z_g^{wgs84}(L,h) = \frac{\gamma(L)}{g_0}h\left[1-\frac{h}{R_e}(1+f+m-2f\sin^2 L)+\frac{h^2}{R_e^2}\right] \tag{4}$$

TABLE 2
Subset of WGS84 Constants

Constant	Value	Constant	Value
Ω	7.292115×10^{-5} rad s^{-1}	μ	$3.986004418 \times 10^{14}$ m^{3}s^{-2}
γ_e	9.7803253359 m s^{-2}	γ_p	9.8321849379 m s^{-2}
R_e	6378137 m	R_p	6356752.3142 m

where R_e denotes the WGS84 equatorial radius, whose value is reported in Table 2 together with other WGS84 constants mentioned in this paper (World Geodetic System and Geomatics Focus Group, 2014). Further terms in Equation (4) are defined as follows (Scherllin-Pirscher et al., 2017):

$$f = \frac{R_e - R_p}{R_e} \quad \text{and} \quad m = \frac{\Omega^2 R_e^2 R_p}{\mu} \tag{5}$$

where R_p is the WGS84 polar radius and Ω and μ are the Earth's nominal mean angular velocity and geocentric gravitational constant, respectively. The gravity at the ellipsoid $\gamma(L)$ according to the so-called Somigliana model is as follows (Scherllin-Pirscher et al., 2017):

$$\gamma(L) = \frac{R_e \gamma_e \cos^2 L + R_p \gamma_p \sin^2 L}{\sqrt{R_e^2 \cos^2 L + R_p^2 \sin^2 L}} \tag{6}$$

where γ_p and γ_e are the polar and equatorial gravitational accelerations at the ellipsoid, respectively. Figure 2(d) shows the difference between h and Z_g^{wgs84} as a function of latitude and geodetic altitude. This difference represents the difference between the geometric and geopotential scales, because both altitudes are referenced to the WGS84 surface. This difference also approximates the differences between H and Z_g^{msl}, because they are both referenced to the MSL surface. The difference between the two scales increases with increasing altitude for a large portion of latitudes centered at the equator, as qualitatively shown in Figure 2(b).

With the following relation (Scherllin-Pirscher et al., 2017), Z_g^{wgs84} can be converted to Z_g^{msl}:

$$Z_g^{\text{msl}}(L, \lambda, H) = Z_g^{\text{wgs84}}(L, h) - N_g(L, \lambda) \tag{7}$$

where $N_g(L, \lambda)$ is the geopotential altitude of the Geoid above the ellipsoid, i.e., the Geoid undulation on a geopotential scale. This term is computed as follows:

$$N_g(L, \lambda) = Z_g^{\text{wgs84}}\left(L, N(L, \lambda)\right) \tag{8}$$

This computation of the geopotential altitude AMSL from the geodetic coordinates is helpful when using weather data, as weather services generally provide altitude information in terms of the geopotential altitude AMSL.

There are more accurate methods for solving Equation (2) than the approach described in the paragraphs above (Scherllin-Pirscher et al., 2017; World Geodetic System and Geomatics Focus Group, 2014). Equation (4) originates from a truncation of a Taylor-series expansion along altitude (World Geodetic System and Geomatics Focus Group, 2014). For this reason, as the altitude increases, the

geopotential altitude AMSL computed from the methodology described in this section will increasingly deviate from the corresponding altitude obtained by more accurate methods. For example, the deviations between the described method and a more accurate approach described by Scherllin-Pirscher et al. (2017) can reach 0.6 m (depending on latitude and longitude) at typical civil aviation cruise altitudes. However, such methods have a significantly greater computational complexity.

2.2 | Pressure Altitude

Pressure (or barometric) altitude can be obtained from measurements performed by a barometer. ICAO (1993) defines this parameter as air pressure, expressed as the altitude that corresponds to that pressure according to the *ICAO Standard Atmosphere*. This atmosphere model coincides with the International Organization for Standardization (ISO) *Standard Atmosphere* (International Organization for Standardization [ISO], 1975), that is the ISA, for geopotential altitude AMSL below 32 km (American Institute of Aeronautics and Astronautics [AIAA], 2010). These models divide the atmosphere into several vertical sections with respect to Z_g^{msl} and provide mathematical descriptions of how temperature and pressure vary within these sections. The next paragraphs briefly present the derivation of two expressions of the pressure altitude (or *hypsometric*) equation for two of these sections between 0 and 20 km.

Considering the atmosphere as a perfect gas and under the assumption of aerostatic equilibrium, the relation between static air pressure and altitude can be expressed by the following differential equation (ICAO, 1993):

$$\mathrm{d}Z_g^{msl} g_0 = \frac{-R_{dry} T}{p}\,\mathrm{d}p \tag{9}$$

where $\mathrm{d}Z_g^{msl}$ is an infinitesimal change in geopotential altitude AMSL, $\mathrm{d}p$ is the corresponding vertical change in static air pressure, and R_{dry} denotes the gas constant of dry air, whose value is reported in Table 3. This table contains the ISA constants and derived quantities mentioned in this section. By making use of the standard ISA model, one can solve Equation (9) analytically. For Z_g^{msl} ranging between 0 and 20 km, the ISA model assumes that the static air temperature varies with respect to Z_g^{msl} as follows:

$$\begin{aligned} T &= T_0 - \alpha Z_g^{msl}, && \text{for } 0 < Z_g^{msl} \le 11 \text{ km} \\ T &= T_1, && \text{for } 11 < Z_g^{msl} \le 20 \text{ km} \end{aligned} \tag{10}$$

where T_0 and T_1 are the ISA (assumed) constant air temperature at MSL and at 11 km, respectively. The term α is the ISA temperature lapse rate, i.e., the assumed constant gradient of temperature over geopotential altitude (ICAO, 1993). Applying Equation (10) in Equation (9) yields the following:

$$\begin{aligned} \mathrm{d}Z_g^{msl} g_0 &= \frac{-R_{dry}\left(T_0 - \alpha Z_g^{msl}\right)}{p}\,\mathrm{d}p, && \text{for } 0 < Z_g^{msl} \le 11 \text{ km} \\ \mathrm{d}Z_g^{msl} g_0 &= \frac{-R_{dry} T_1}{p}\,\mathrm{d}p, && \text{for } 11 < Z_g^{msl} \le 20 \text{ km} \end{aligned} \tag{11}$$

Integrating Equation (11) along $Z_{\mathrm{g}}^{\mathrm{msl}}$ from a certain reference geopotential altitude AMSL $Z_{\mathrm{g,ref}}^{\mathrm{msl}}$, or from 11 km, leads to the following:

$$\begin{aligned} Z_{\mathrm{p}}^{\mathrm{msl}} &= \frac{T_{\mathrm{ref}}}{\alpha}\left[1-\left(\frac{p}{p_{\mathrm{ref}}}\right)^{\frac{\alpha R_{\mathrm{dry}}}{g_0}}\right]+Z_{\mathrm{g,ref}}^{\mathrm{msl}}, \quad \text{for } 0<Z_{\mathrm{g}}^{\mathrm{msl}}\leq 11\ \mathrm{km} \\ Z_{\mathrm{p}}^{\mathrm{msl}} &= 11\ \mathrm{km}-\frac{T_1 R_{\mathrm{dry}}}{g_0}\ln\left(\frac{p}{p_1}\right), \quad \text{for } 11<Z_{\mathrm{g}}^{\mathrm{msl}}\leq 20\ \mathrm{km} \end{aligned} \tag{12}$$

In Equation (12), we modify the notation of the altitude output from $Z_{\mathrm{g}}^{\mathrm{msl}}$ to $Z_{\mathrm{p}}^{\mathrm{msl}}$ to highlight that this geopotential altitude is not the true geopotential altitude AMSL. It is instead the geopotential altitude AMSL that can be estimated with a pressure measurement and the ISA model, i.e., the pressure altitude. The variables T_{ref} and p_{ref} denote the temperature and pressure at $Z_{\mathrm{g,ref}}^{\mathrm{msl}}$, respectively. With p_1, we denote the assumed constant value of air pressure at $Z_{\mathrm{g}}^{\mathrm{msl}}=11$ km. This value was derived by ICAO (1993) by projecting the (assumed) constant MSL air pressure p_0 to $Z_{\mathrm{g}}^{\mathrm{msl}}=11$ km. The values of p_0 and p_1 are both given in Table 3.

Equation (12) can be adapted to also consider the effect of air humidity within the hypothesized aerostatic equilibrium. This adaptation consists of substituting the ambient temperature values with their corresponding ambient virtual temperatures (Giez et al., 2017). The virtual temperature T_{v} corresponding to an actual temperature T is defined as follows:

$$T_{\mathrm{V}} = T\left[1+\left(\frac{R_{\mathrm{vap}}}{R_{\mathrm{dry}}}-1\right)q\right] \tag{13}$$

where q denotes the specific humidity, i.e., the mass of water vapor per kilogram of moist air, and $R_{\mathrm{vap}}=461.51\ \mathrm{J\ kg^{-1}\ K^{-1}}$ is the specific gas constant of water vapor (Giez et al., 2017).

The QNE pressure altitude is obtained from Equation (12) by setting the ISA MSL isobar as the reference isobar surface (ICAO, 1993; RTCA, 2020), which consists of setting $Z_{\mathrm{g,ref}}^{\mathrm{msl}}=0$, $T_{\mathrm{ref}}=T_0$, and $p_{\mathrm{ref}}=p_0$ in the first expression of Equation (12):

$$Z_{\mathrm{p}}^{\mathrm{qne}} = \frac{T_0}{\alpha}\left[1-\left(\frac{p}{p_0}\right)^{\frac{\alpha R_{\mathrm{dry}}}{g_0}}\right] \tag{14}$$

Therefore, the QNE pressure altitude is an estimate of the actual geopotential altitude above the p_0 isobar surface, i.e., the ISA MSL isobar. The true pressure and temperature at MSL generally deviate from the constant values assumed by the ISA

TABLE 3
Subset of ISA Constants and Derived Quantities

Constant	Value	Constant	Value
R_{dry}	$287.05287\ \mathrm{J\ kg^{-1}\ K^{-1}}$	α	$6.5\ \mathrm{K\ km^{-1}}$
T_0	288.15 K	T_1	216.65 K
P_0	101.325×10^3 Pa	P_1	22.632×10^3 Pa

model, and the QNE pressure altitude will thus deviate in proportion from the true geopotential altitude AMSL. Moreover, the pressure altitude can still differ remarkably from the true geopotential altitude AMSL, even if the actual MSL values for temperature and pressure are used. This deviation arises from the inherent ISA model approximation of the actual atmosphere dynamics.

3 | BAROMETRIC GEODETIC ALTITUDE COMPUTATION METHODOLOGY

Figure 3 summarizes our methodology for deriving an accurate geodetic altitude from airborne barometric pressure measurements and external weather data. The steps of this methodology are described in the current section.

3.1 | Weather-Corrected Pressure Altitude and Weather Data

We define the *weather-corrected pressure altitude*, $Z_{\mathrm{p,w}}^{\mathrm{msl}}$, as the pressure altitude AMSL obtained from weather data. We obtain this parameter from the first of the two expressions of the pressure altitude equation (i.e., Equation (12)) when the actual, non-ISA air pressure $p_{\mathrm{w,user}}$ and temperature $T_{\mathrm{w,user}}$ at the estimated user's horizontal location and geopotential altitude AMSL are employed as p_{ref} and T_{ref}. Accordingly, the estimated user's $Z_{\mathrm{g}}^{\mathrm{msl}}$ is used as $Z_{\mathrm{g,ref}}^{\mathrm{msl}}$. For the sake of clarity, we provide an explicit expression of the weather-corrected pressure altitude equation:

$$Z_{\mathrm{p,w}}^{\mathrm{msl}} = \frac{T_{\mathrm{w,user}}}{\alpha}\left[1-\left(\frac{p}{p_{\mathrm{w,user}}}\right)^{\frac{\alpha R_{\mathrm{dry}}}{g_0}}\right] + Z_{\mathrm{g}}^{\mathrm{msl}} \tag{15}$$

Weather data can be used within the second of the two expressions of Equation (12) when the user is above a geopotential altitude AMSL of 11 km. In that case, the actual air pressure at $Z_{\mathrm{g}}^{\mathrm{msl}} = 11$ km, $p_{11\,\mathrm{km}}$, is used instead of p_1. Analogously, the actual air temperature at 11 km, $T_{11\,\mathrm{km}}$, is used instead of T_1. To consider the effects due to air humidity, the temperature parameters T_{ref} and $T_{11\,\mathrm{km}}$ are substituted in Equation (12) with their corresponding virtual temperatures $T_{\mathrm{V,ref}}$ and $T_{\mathrm{V,11\,km}}$. These terms can be computed from Equation (13). In this case, the actual specific humidity at the user's horizontal and geopotential altitude location AMSL $q_{\mathrm{w,user}}$, or $q_{11\,\mathrm{km}}$ for $Z_{\mathrm{g}}^{\mathrm{msl}} = 11$ km, is used in Equation (13). We found that the consideration of specific humidity through Equation (13) had a negligible impact in the weather-corrected pressure altitude equation when evaluated with the flight data described in Section 4.1. Moreover, utilizing the second

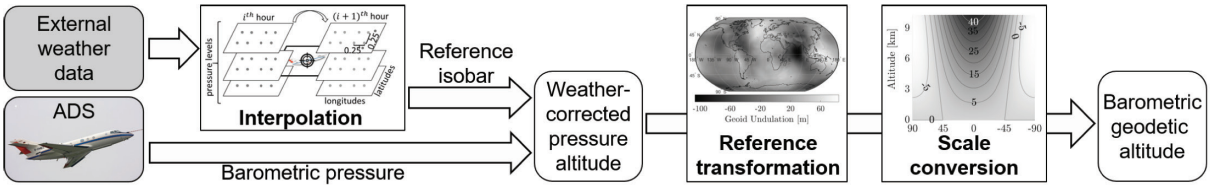

FIGURE 3 Barometric geodetic altitude computation scheme

of the two expressions of Equation (12) at a geopotential altitude AMSL above 11 km produced only negligible differences with respect to using the first of the two expressions in those instances. For this reason, we base the weather-corrected pressure altitude computation (i.e., Equation (15)) on the first of the two expressions of Equation (12) only.

Estimates of the actual values of $(p, T, q)_{\text{w,user}}$ (or $(p, T, q)_{\text{weath,11km}}$) may be obtained from weather forecast services for real-time navigation or from climate reanalyses for offline applications. A climate reanalysis depicts past weather in the currently most complete way possible. The reanalysis is a combination of measurements with past short-range weather forecasts, recomputed with the latest weather forecasting models (European Center for Medium-Range Weather Forecasts [ECMWF], 2020). In this work, we used weather data from the ECMWF Reanalysis v5 (ERA5) (Hersbach et al., 2023) provided by the European Center for Medium-range Weather Forecast (ECMWF). ERA5 was started in 2016 and, since 2017, has always lagged 2–3 months behind the present. A backward reanalyis to 1940 was also performed by ECMWF. Since 2019, ECMWF has also made available an ERA5 subset known as ERA5T. This subset provides preliminary data for ERA on a daily basis, with only a 5-day delay with respect to the present. This relationship is summarized in Figure 4(a). ERA5 data can be publicly retrieved for 37 pressure levels ranging from 1000 to 1 hPa. Data are provided for each UTC full hour on a global regular longitude–latitude grid with a resolution of 0.25°. Thus, the weather data set can be visualized as a four-dimensional (4D) array of points, with dimensions of longitude, latitude, pressure level, and time, as shown in Figure 4(b). For each point in this 4D array, the temperature, geopotential altitude AMSL, and specific humidity are provided, along with other weather parameters. Consequently, multidimensional interpolation of the ERA5 data is necessary to obtain the temperature, pressure, and specific humidity at the location of the user. In this work, we applied linear interpolation in both the time domain and the horizontal plane. For the vertical domain, we applied linear interpolation for temperature and specific humidity and logarithmic interpolation for pressure, as suggested by Giez et al. (2017).

Our analyses consider a nominal situation in which the assumed developments of temperature and pressure, which are consistent with the ISA, provide a good representation of the true atmosphere. Because we interpolate weather data that are expected to be a good estimate of the real weather, we minimize the impact of potential non-compliance of the model with the real atmosphere. In the future, systematic analyses on available weather data may allow us to gain information about the recurrence and potential impact of unexpected weather behaviors.

Equation (12), and thus Equation (15), is based on the ISA model. As explained in Section 3.1, this model assumes that the air temperature decreases linearly

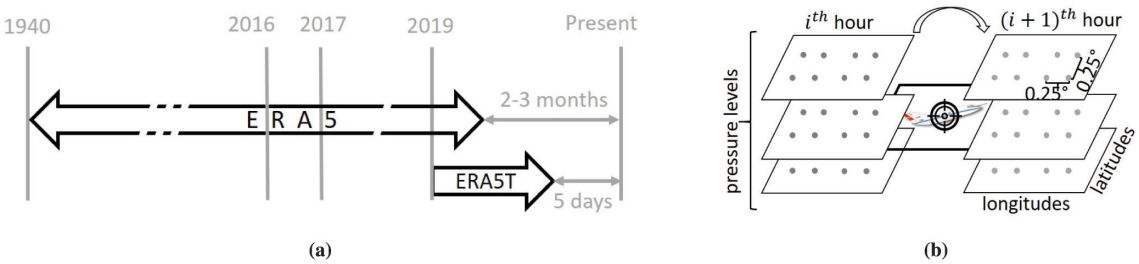

FIGURE 4 ECMWF weather reanalysis data sets and their structure (a) Overview of the considered ECMWF weather data sets (b) 4D structure of retrieved ECMWF weather data

with increasing geopotential altitude AMSL, with a constant gradient termed the lapse rate, denoted by α. By using weather data for different pressure levels, one may obtain local values for α considering the temperatures and altitudes of two vertically adjacent pressure levels. These local values of α may then be used in Equation (15). However, we observed that this approach produces negligible differences with respect to the method utilized in this work. These two approaches give similar results because the approach of deriving and using a local α is implicitly the same operation as performing the above-described multidimensional interpolation of weather data temperature.

3.2 | Conversion from Weather-Corrected Pressure Altitude to Geodetic Altitude

The weather-corrected pressure altitude $Z_{\mathrm{p,w}}^{\mathrm{msl}}$ is an estimate of the true geopotential altitude AMSL, $Z_{\mathrm{g}}^{\mathrm{msl}}$. Table 1 classifies altitude definitions according to their references and scales. The geopotential altitude AMSL and geodetic altitude differ by reference and scale. If a geopotential altitude AMSL is known, then the corresponding geodetic altitude h may be obtained by applying a two-step conversion. First, the reference must be adjusted from the MSL to the Earth ellipsoid; secondly, the scale must be converted from geopotential to geometric. To transform the reference from MSL to the ellipsoid, we solve Equation (7) for the user's barometric geopotential altitude above the WGS84 ellipsoid, $Z_{\mathrm{p,w}}^{\mathrm{wgs84}}$, by which we denote the $Z_{\mathrm{g}}^{\mathrm{wgs84}}$ obtained from the weather-corrected pressure altitude. In this first step, $Z_{\mathrm{p,w}}^{\mathrm{msl}}$ corresponds to $Z_{\mathrm{g}}^{\mathrm{msl}}$. In the second step, Equation (4) is used to convert $Z_{\mathrm{p,w}}^{\mathrm{wgs84}}$ to the geodetic altitude. Because this step cannot be performed analytically, we solve Equation (4) for h numerically instead:

$$h_{\mathrm{Baro}} = \arg\min_{h}\left(\left|Z_{\mathrm{p,w}}^{\mathrm{wgs84}} - Z_{\mathrm{g}}^{\mathrm{wgs84}}(h)\right|\right) \tag{16}$$

where $Z_{\mathrm{g}}^{\mathrm{wgs84}}(h)$ is the right-hand side of Equation (4) evaluated at the given latitude. This iterative nonlinear minimization problem is initialized by assuming $Z_{\mathrm{p,w}}^{\mathrm{wgs84}}$ as the first approximation for h. The output of this step is the barometric geodetic altitude, which we denote as h_{Baro}.

Algorithm 1 presents a summary of the methodology for deriving the barometric geodetic altitude from barometric pressure measurements and external weather data. Lines 1–3 pertain to the computation of weather-corrected pressure altitude. The conversion to geodetic altitude is covered in lines 4–5.

ALGORITHM 1
Computation of barometric geodetic altitude

Require: User's barometric pressure measurement p and estimated coordinates L, λ, h at time t
Require: 4D weather data arrays of temperature and geopotential altitude AMSL

1: $Z_{\mathrm{g}}^{\mathrm{msl}} \leftarrow$ User's estimated geopotential altitude AMSL computation	▷ Equations (4) and (7)
2: $(p, T)_{\mathrm{w,user}} \leftarrow$ Weather data interpolation to user's estimated location	▷ Section 3.1
3: $Z_{\mathrm{p,w}}^{\mathrm{msl}} \leftarrow$ User's weather-corrected pressure altitude computation	▷ Equation (15)
4: $Z_{\mathrm{p,w}}^{\mathrm{wgs84}} \leftarrow$ Altitude reference transformation to WGS84	▷ Equation (7), solved for $Z_{\mathrm{g}}^{\mathrm{wgs84}}$
5: $h_{\mathrm{Baro}} \leftarrow$ Scale conversion to geometric	▷ Equation (16)

4 | ERROR AND THREAT MODELING OF BAROMETRIC GEODETIC ALTITUDE

4.1 | Experimental Flight Data

The analyses of this work are based on measurements made during nine flights performed between the 9th and 13th of July 2018 (Osechas et al., 2019). The flights were performed with the Dassault Falcon 20–E5 jet aircraft of the German Aerospace Center (DLR), as shown in Figure 5. The vertical and horizontal developments of the flight trajectories are shown in Figure 6(a) and Figure 6(b), respectively. The color shading from grey to black in Figure 6(b) is proportional to the elapsed time since take-off. For all flights, the departure and destination airport was the Oberpfaffenhofen Airport (ICAO Code: EDMO) adjacent to the DLR site in Oberpfaffenhofen.

The analyses of this paper only focus on the flight sections for which barometric pressure measurements were available. Each of these sections covers most of each flight, with the exception of short intervals at the initial and final portions of the flights. A total of approximately 20 h of barometric pressure measurements was recorded at 10 Hz. GNSS data were recorded in parallel and were used after precise post-processing as ground truth. We also apply weather data interpolation along this trajectory.

4.2 | Geodetic Altitude Computation Accuracy

The deviations of the QNE pressure altitude from the true geodetic altitude along the nine investigated test flights are shown in Figure 7 in blue. The errors of the computed (barometric) geodetic altitude are shown in black in the same figure, adopting the same color code as Figure 1 for different altitudes. Figure 7 shows that the barometric geodetic altitude is remarkably closer to the true geodetic altitude than the QNE pressure altitude, if the latter is interpreted as the geodetic altitude. Furthermore, comparing Figure 7 with Figure 6(a) shows a certain level of modulation between the QNE pressure altitude deviations and the true geodetic altitude profiles. Indeed, it can be noted that the deviations generally increase with increasing altitude. Nonetheless, the development of deviations along the third flight differs from this general observed tendency. A possible reason for this difference may lie in the way flight guidance itself is enabled. As mentioned in Section 1, vertical aircraft guidance is based on FLs, which means that aircraft at cruise altitudes fly

FIGURE 5 DLR's Dassault Falcon 20–E5, with an enlarged view of a static pressure port and Pitot tube on each of the two fuselage sides

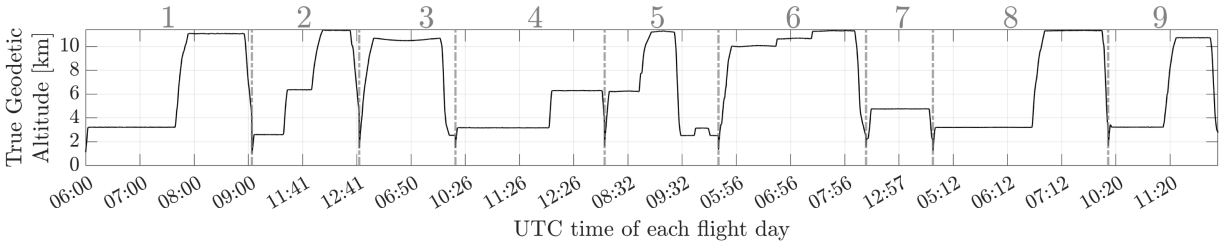

(a)

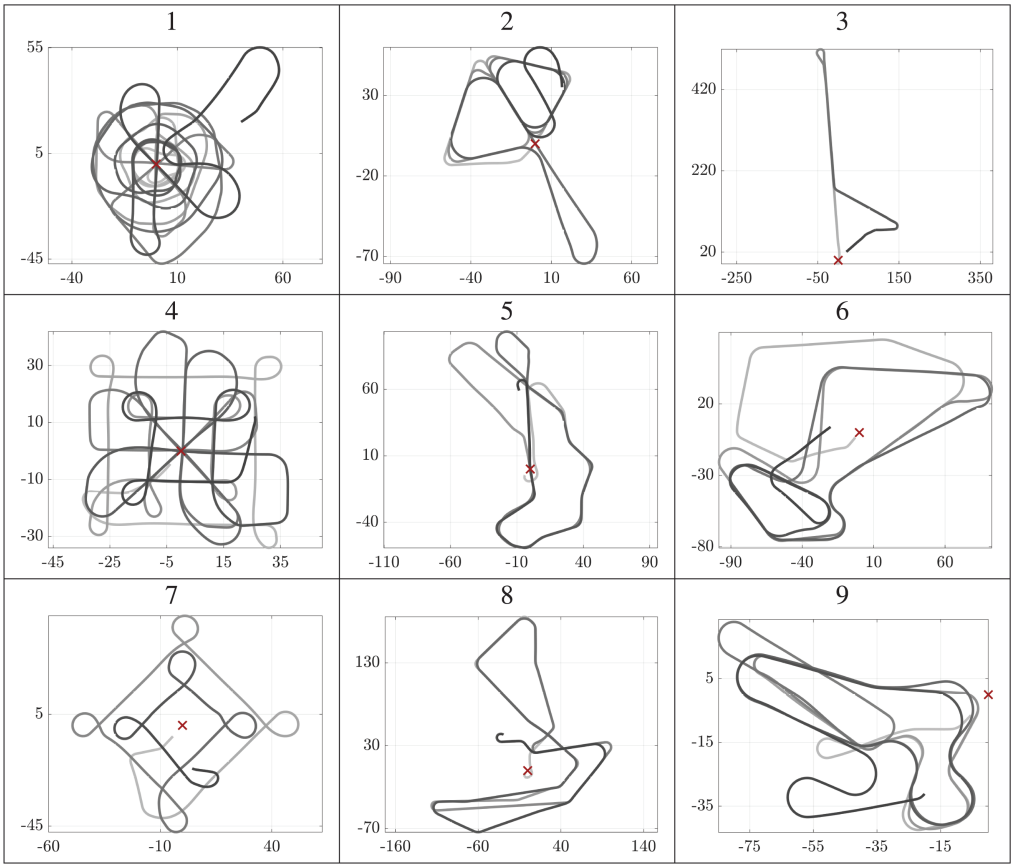

(b)

FIGURE 6 Test flight trajectories (a) True geodetic altitude profiles (b) Trajectories in a local planar frame centered at the EDMO airport (red cross), with the y and x axes directed north and east, respectively, in kilometers

along isobar surfaces. These surfaces can be more or less detached from surfaces of constant geodetic altitude, depending on the location and time. This detachment may produce the aforementioned development in altitude deviations, especially along flights spanning larger horizontal distances, such as Flight 3.

The errors in barometric geodetic altitude increase during instances of steep altitude transitions, which hints at a dependency on flight dynamics.

4.3 | Mitigation of Dynamics-Induced Error Components

We detected a roughly linear relationship between the barometric geodetic altitude errors and the aircraft's pitch attitude angle, as illustrated in Figure 8(a). This finding complies with our previous observation that the errors increase during

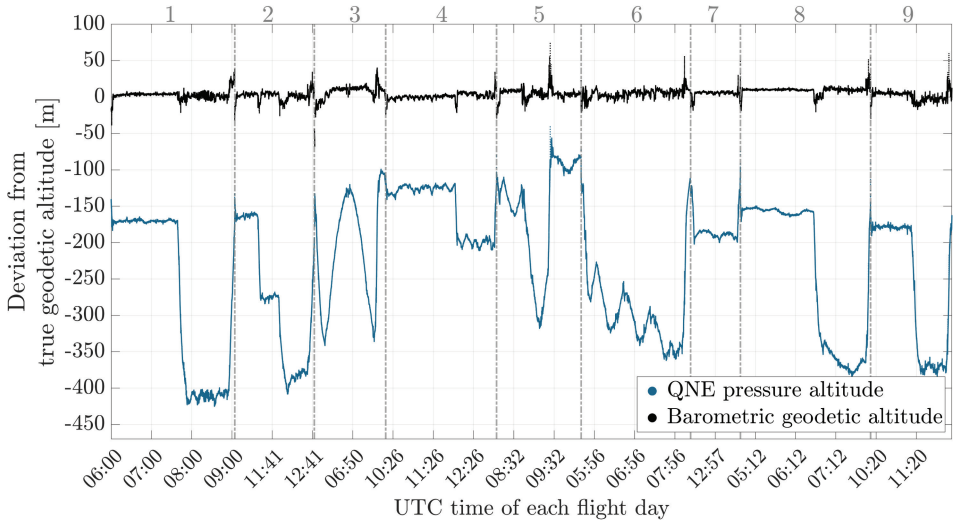

FIGURE 7 Deviation in QNE pressure altitude and barometric geodetic altitude from the true geodetic altitude

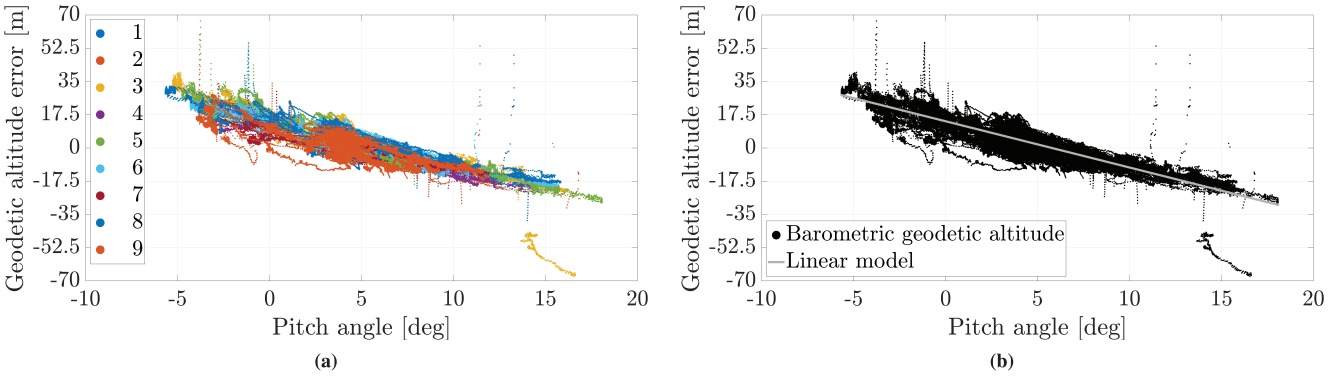

FIGURE 8 Relationship between barometric geodetic altitude errors and pitch attitude angle (a) Altitude errors versus pitch angle for each of the nine flights (b) Linear model relating the altitude errors and pitch angle

instances of non-negligible altitude variations. Indeed, altitude variations are generally associated with variations in aircraft pitch attitude. The inflow direction of air into the pressure ports may vary depending on the pitch angle and may affect air pressure measurements. This would consequently affect the barometric geodetic altitude measurements as well. We obtained a linear model relating the errors and pitch attitude angle through a robust linear regression using a bisquare fitting weighting function. Thus, the outliers, e.g., those at approximately −4° and −1°, have a negligible influence on the derivation of the model. The model is described by $\Delta h(\theta) = m\theta + n$ whereby the model parameters were found to be $m = -2.44$ m deg^{-1} and $n = 14.47$ m. Figure 8(b) shows the linear model for different pitch angles.

We note that this type of linear model may vary depending on the employed aircraft and/or the installed sensor and its specific calibration. However, an approach similar to the method presented herein could potentially still be followed. Furthermore, any effect that might alter the local pressure around measuring ports could have an impact on the measured static pressure and, therefore, on the barometric geodetic altitude. In the available experimental data, we did not find any clear relationship between altitude errors and other parameters, such as

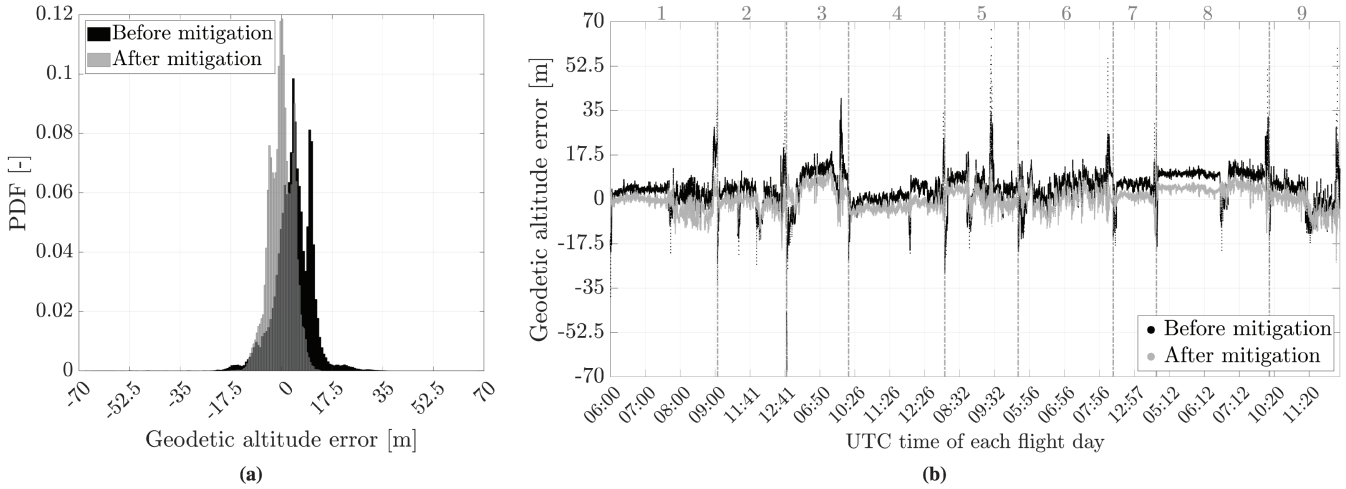

FIGURE 9 Mitigation of dynamics-induced effects by means of the pitch-angle-based model (a) Effect of mitigation on the error distribution (b) Altitude errors, before and after mitigation with a linear model based on pitch angle

the cross wind. However, we cannot exclude the possibility that other relationships may be found in measurements performed by other types of sensors/airplanes and/or under different weather conditions.

Figures 9(a) and 9(b) show a comparison of the altitude errors before and after the application of mitigation based on the pitch angle in the probability density function (PDF) and time domain, respectively. In Figure 9(b), it is apparent that this mitigation can reduce the magnitude of large errors, particularly during altitude variation phases. Accordingly, the values of the mean and standard deviation improved from approximately 4.6 m and 6.4 m to approximately –0.1 m and 4.1 m, respectively. This decrease in these parameters is reflected in Figure 9(a).

4.4 | Nominal Error Models

It is required that a nominal error model for integrity be an upper bound for all possible errors, with the exception of 10^{-7} of cases at most. Gaussian error models can be easily considered in linear estimators (e.g., least-squares) because they preserve their distribution through convolution. Thus, a Gaussian distribution can be used to bound the residual error distribution. We derived a Gaussian overbound in the cumulative density function (CDF) sense by applying the approach of Blanch et al. (2019). We applied this method to the sample distribution consisting of residual errors in the barometric geodetic altitude along the aforementioned nine flights and after the pitch-angle-based mitigation. We then identified the standard deviation, $\sigma_{\text{int,Baro}}$, and the nominal bias, $b_{\text{nom,Baro}}$, used for integrity with the standard deviation and bias of the derived Gaussian overbound, respectively. The values of the parameters found with this approach are $\sigma_{\text{int,Baro}} = 15$ m and $b_{\text{nom,Baro}} = 1.2$ m.

We also used the aforementioned sample distribution to determine the nominal error model parameter for accuracy and continuity, $\sigma_{\text{acc,Baro}}$. We derived this by fitting to the sample distribution a zero-mean Gaussian distribution that bounds 95% of the residual error distribution, which yielded $\sigma_{\text{acc,Baro}} = 4.465$ m. Figure 10 shows the folded CDFs of the residual error distribution and of the distributions corresponding to the empirical nominal error models.

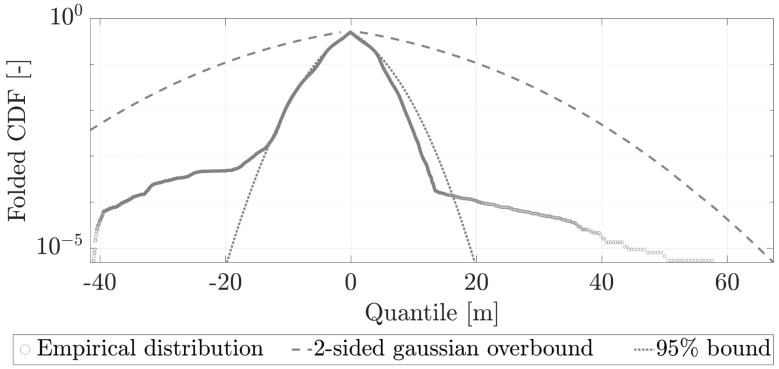

FIGURE 10 Nominal error models for integrity (Gaussian overbound) and for accuracy and continuity (95% bound)

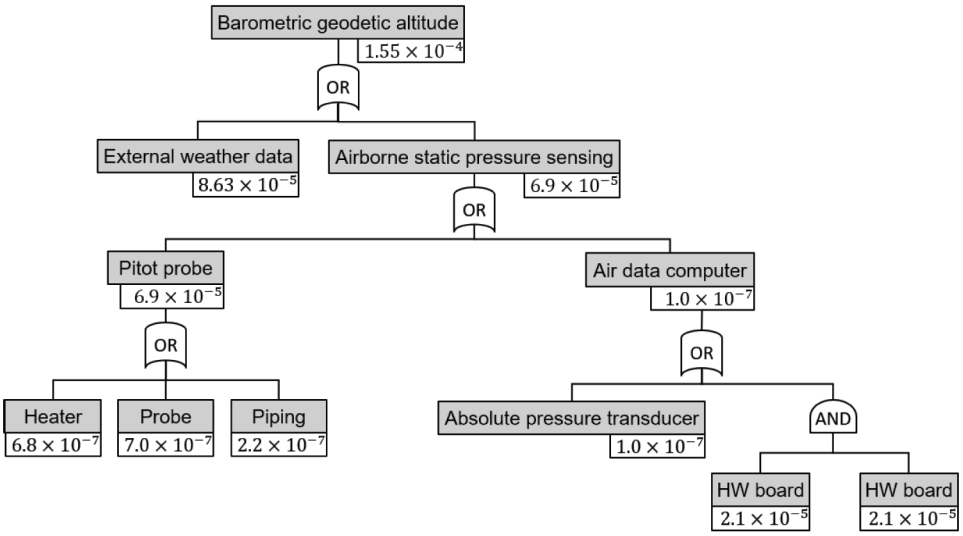

FIGURE 11 Fault tree (based on work by Lerro & Battipede (2021)) of the barometric geodetic altitude
The fault rates of all involved systems and parts are given in the white boxes, with the unit of measure being h^{-1}.

4.5 | Threat Model

The threat model is based on the probability of fault in the computation of the barometric geodetic altitude, P_{Baro}. This probability can be identified from the fault rate, in terms of cases per hour. The fault propagation to the barometric geodetic altitude can be investigated through a fault tree analysis with two top-level branches, as depicted in Figure 11. The right branch is related to the airborne barometric pressure measurement. The left branch is related to the external weather data employed for the pressure altitude correction.

The airborne side, based on work by Lerro & Battipede (2021), may be broken down to the hardware (HW) ADS parts, which are involved in the execution and analog-to-digital conversion of the barometric pressure measurements. Lerro & Battipede (2021) focused on an ADS designed for use cases in the small aircraft transportation (SAT) sector. The ADS is decomposed down to the probe, piping, and heater of the Pitot tube and down to the pressure transducer and the two HW boards (one being redundant) that are part of the ADC. The fault rates of the single

parts and subsystems were obtained from Quanterion Solutions Incorporated (2016), which provides statistical data for a multitude of electronic, mechanical, and electromechanical components. The fault rate in the airborne branch can then be computed, starting from the lowest levels, based on a bottom–up system safety assessment approach. This yields a fault rate of 6.91×10^{-5} h^{-1}. The fault rates of all involved systems and parts are given in Figure 11, in which the unit of measure, i.e., h^{-1}, is omitted. Adopting this airborne fault rate for airplanes in the transport category, which is classified in accordance with European Union Aviation Safety Agency (EASA) CS-25 or Federal Aviation Administration 14 CFR Part 25, can be considered a conservative approach. In fact, it is expected that EASA CS-25-classified airplanes are provided with ADSs of a higher grade with respect to EASA CS-23-classified airplanes, such as SAT aircraft (Di Vito et al., 2021; Lerro & Battipede, 2021; Piwek & Wiśniowski, 2016).

The Baro augmentation is meant to be adopted in an operational scenario. In such a scenario, the external weather data used for pressure altitude correction must be weather forecast data. We have made use of climate reanalysis data instead, specifically data from the ECMWF ERA5 climate reanalysis (Hersbach et al., 2023). ECMWF provides a list of documented, known, solved or unresolved issues in the ERA5 reanalysis and in its ERA5T subset (Hersbach et al., 2023). We consider the list of issues in the ERA5T subset for deriving an estimate of the weather data fault rate, because ERA5T is much closer to real time than ERA5. Based on this list, it is possible to count the issues that can be considered as weather data faults within the context of the weather-corrected pressure altitude computation. We compute the fault rate in the weather data from the number of weather data faults and the time span covered by the weather data. This approach is based on the methodology described by Walter et al. (2019) for the determination of GNSS fault rates for ARAIM. In the case of ERA5T, we considered that none of the reported issues could potentially cause a fault in the pressure altitude correction. Nonetheless, we conservatively increased the number of ERA5T faults by 2, as suggested by Walter et al. (2019). A time span must be defined for deriving the fault rate with this approach. We considered the time span from the ERA5T release date to the 23rd of March 2023, i.e., when we carried out this analysis. This methodology returns a value of 8.63×10^{-5} h^{-1} for the weather data fault rate.

Considering the airborne and weather data sides of the fault tree, the value of the estimated fault rate in the barometric geodetic altitude is ultimately 1.55×10^{-4} h^{-1}. This value is reported in the top level of Figure 11.

Within this section, we have implicitly assumed that the derived linear mitigation model presented in Section 4.3 pertains to the nominal model and behavior. For now, we consider the non-compliance with the nominal error model to be a result of calibration/processing fault and, as such, to be included in the threat model. These faults could arise, for example, during instances of turbulent vertices around the pressure ports. In this work, we have not isolated calibration faults from faults related to other ADS pressure-measuring functions. Thus, we consider these faults within the same block in the integrity tree (top-level right branch in Figure 11). We assume that the integrity monitoring function of our proposed ARAIM-based integration of barometric altitude with GNSS (see Section 5) is able to capture such faults. Analyses of the processing of Section 5 have indeed shown that one of the monitored fault modes is represented by faults in the part of the architecture providing barometric geodetic altitude measurements. As this paper provides a first description of a barometer- and weather-data-augmented GNSS-based navigation system, future developments of this work will investigate details such as potential solutions for isolating different types of pressure measurement faults.

5 | BARO-AUGMENTED ARAIM

This section describes the integration of barometric geodetic altitude with GNSS within the ARAIM algorithm. This concept is summarized in Figure 12(a), where a single block includes all processing steps of the flow diagram shown in Figure 3.

In this paper, this integration is referred to as *Baro augmentation*. Analogously, the resulting algorithm is herein named *Baro-augmented ARAIM*. For the sake of brevity, we refer to this algorithm as *Baro ARAIM* in some instances. At this stage of research, the pitch-angle-based mitigation (see Section 4.3) cannot yet be generalized within an architecture that is meant to be common to different types of aircraft. Therefore, this mitigation is not included in the flow diagram of Figure 12(a). Nevertheless, in our assessment with real flight data (see Section 5.2), we provided the ARAIM-based integration block with the barometric geodetic altitude after the aforementioned mitigation. As a final remark, this work only considers GPS and Galileo GNSS constellations, as shown in Figure 12(a).

The next paragraphs describe the modifications introduced by the Baro augmentation in the main equations of the baseline ARAIM. The latter is briefly summarized in Appendix A. Figure 12(b) presents a visual summary of the parameters required for the Baro augmentation and where they play a role in the Baro-augmented ARAIM algorithm.

The inclusion of barometric measurements in the typical WLS GNSS positioning algorithm and ARAIM is achieved by augmenting the vector $\Delta\mathbf{z}$ in Equation (A1) by one element. This element is the difference between the barometric geodetic altitude measurement and the latest user geodetic altitude estimate:

$$\Delta\mathbf{z}_{\text{Baro-ARAIM}} = \begin{bmatrix} \Delta\boldsymbol{\rho} \\ h_{\text{Baro}} - \hat{h} \end{bmatrix} \tag{17}$$

with the subscript *Baro ARAIM* featuring all ARAIM parameters that are modified by the Baro augmentation. As a result, the geometry matrix in the east–north–up (ENU) frame is also augmented by one additional row:

$$\mathbf{H}_{\text{Baro-ARAIM}} = \begin{bmatrix} \mathbf{H} \\ \mathbf{H}_{\text{Baro}} \end{bmatrix} \text{ with } \mathbf{H}_{\text{Baro}} = \begin{bmatrix} 0 & 0 & 1 & 0 & 0 \end{bmatrix} \tag{18}$$

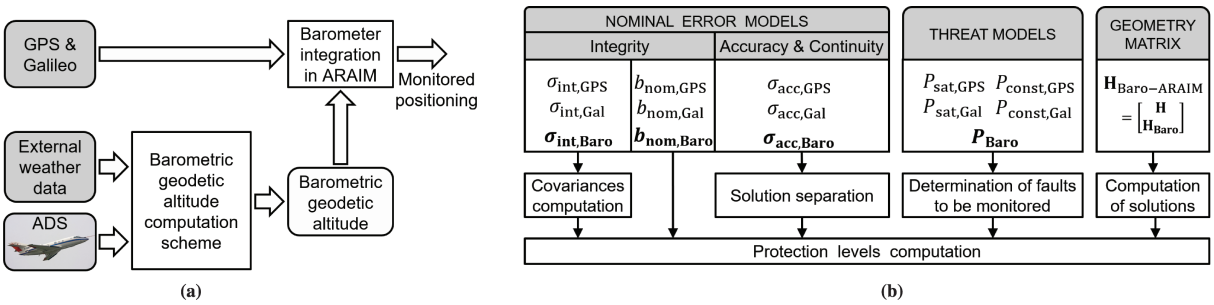

FIGURE 12 Baro-augmented ARAIM: integration of barometric geodetic altitude within the baseline ARAIM algorithm (a) Flow diagram of the integration of barometric measurements and weather data with GNSS ARAIM (b) Key parameters in the Baro-augmented ARAIM. The parameters in bold font and with *Baro* in their subscript are required in addition to those needed in the baseline ARAIM.

The integration of the barometric geodetic altitude into ARAIM requires the definition of corresponding nominal error models and a threat model. The measurement covariance matrix used for integrity is augmented with the nominal error model for integrity:

$$\boldsymbol{\Sigma}_{\text{Baro–ARAIM}} = \begin{bmatrix} \boldsymbol{\Sigma} & \mathbf{0} \\ \mathbf{0} & \boldsymbol{\Sigma}_{\text{Baro}} \end{bmatrix} \text{ with } \boldsymbol{\Sigma}_{\text{Baro}} = \sigma^2_{\text{int,Baro}} \tag{19}$$

The threat model of the barometric geodetic altitude measurement is based on the probability of fault of the system that produces the barometric geodetic altitude measurements, i.e., P_{Baro}. With this, the subset determination described in Appendix A is modified by simply extending Equation (A4) with the following:

$$P_{\text{event},N_{\text{meas}}+N_{\text{const}}+1} = P_{\text{Baro}} \tag{20}$$

The nominal error and threat models derived in Section 4 are employed in the current section for the purpose of augmenting GNSS with the barometric geodetic altitude.

5.1 | Availability Simulations

We first assessed the performance of the Baro augmentation by means of availability simulations of the localizer performance with vertical guidance (LPV) service. In particular, we focused on LPV operations with guidance down to a height of 200 ft (above the runway threshold), which is denoted by LPV-200. These are the target operations of Working Group C (2016). For this purpose, we made use of the GNSS constellation simulations and multiple-hypothesis solution separation (MHSS) computations of the *MATLAB® algorithm availability simulation tool* (Walter & Blanch, 2019). This toolset simulates Galileo and GPS constellations along a certain time span T and runs the ARAIM algorithm at every epoch, with a given time step Δt. In particular, the algorithm is run on all grid points of a global longitude–latitude grid with given longitude $\Delta\lambda$ and latitude ΔL steps, respectively. The default values used for the simulation are $T = 86400$ s, $\Delta T = 300$ s, and $\Delta\lambda = \Delta L = 10°$. The satellite elevation mask angle is 5°. For the simulations presented in this section, we refined the grid by setting $\Delta\lambda = \Delta L = 5°$. The criteria for the availability determination, compatible with LPV-200 requirements, are the following: $\text{HPL} \leq \text{HAL} = 40$ m, $\text{VPL} \leq \text{VAL} = 35$ m, $\text{EMT} \leq 15$ m, and $\sigma_{\text{v,acc}} \leq 1.87$ m, where HPL and VPL denote the horizontal and vertical PLs, respectively, and HAL and VAL denote the horizontal and vertical alert limits, respectively. EMT denotes the effective monitoring threshold, and $\sigma_{\text{v,acc}}$ denotes the standard deviation of the vertical position solution. All of these quantities are defined in the work by Blanch et al. (2015).

The values used for the GNSS parameters needed within ARAIM are reported in Table 4, based on the work by Working Group C (2016). For the simulations presented in Section 5.1.2, we employed the empirical error and threat models of Section 4. In Section 5.1.1, we first perform a sensitivity analysis of the availability with respect to other possible values of the error and threat model parameters instead. As mentioned in Appendix A, ARAIM requires the definition of some further constants and design parameters that are related to integrity, accuracy, and continuity. In these simulations, we utilized the default values assigned by Walter & Blanch (2019) to these additional parameters for vertical ARAIM.

TABLE 4
GNSS Parameters Required for ARAIM

	σ_{URA} [m]	σ_{URE} [m]	b_{nom} [m]	P_{sat} [h^{-1}]	P_{const} [h^{-1}]
Galileo	1	2/3	0.75	10^{-5}	10^{-4}
GPS	1	2/3	0.75	10^{-5}	10^{-8}

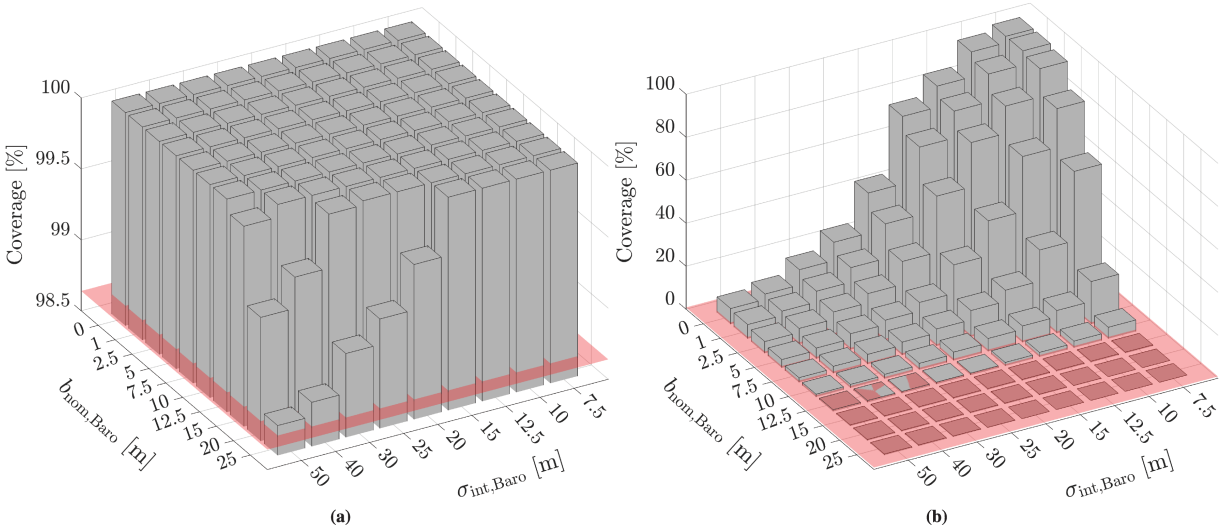

FIGURE 13 World surface coverage for the 99.5 percentile of the LPV-200 availability (with VAL = 35 m on the left and VAL = 20 m on the right) achieved by the Baro ARAIM during one day, as a function of $\sigma_{int,Baro}$ and $b_{nom,Baro}$ (a) World coverage with VAL = 35 m (b) World coverage with VAL = 20 m
The red transparent horizontal planes represent the corresponding coverage levels achieved by the baseline ARAIM.

5.1.1 | Availability Sensitivity to Barometric Error and Threat Models

We ran 90 simulations with the derived threat model and with different values of the error model parameters of the barometric geodetic altitude measurement, with the goal of assessing the impact of these parameters on the worldwide LPV-200 availability achieved by the Baro-augmented ARAIM. The values of these varying parameters can be read from the axes of each of the two subfigures of Figure 13. We set the accuracy model within these simulations as $\sigma_{acc,Baro} = \frac{2}{3}\sigma_{int,Baro}$. This mimics the relationship between the GNSS σ_{acc} and σ_{int} (Working Group C, 2016). We note that the pairs $\{b_{nom,Baro}, \sigma_{int,Baro}\}$ for which $b_{nom,Baro}$ is larger than $\sigma_{int,Baro}$ are unlikely in the real world.

Figure 13(a) allows us to compare the coverage results of the aforementioned 90 simulations with the results for the baseline ARAIM. This figure shows the world coverage for the 99.5 percentile of the LPV-200 service availability over a day, as a function of $\sigma_{int,Baro}$ and $b_{nom,Baro}$. The baseline ARAIM achieves a coverage of 98.64%, which is represented by the red transparent horizontal plane. Notably, the availability achieved with the Baro-augmented ARAIM is higher than that attained with the baseline ARAIM for all of the tested combinations. The coverage achieved with the Baro augmentation is found to be 100% for each of the tested values of $b_{nom,Baro}$ if $\sigma_{int,Baro} \leq 15$ m.

Figure 13(b) is analogous to Figure 13(a), where VAL was decreased from 35 to 20 m. The latter value is the VAL adopted for the approach with vertical

guidance (APV) operations of class APV-II (ICAO, 2018a). This analysis allows us to better portray the coverage improvement provided by the Baro augmentation. With these requirements, the baseline ARAIM achieves a coverage of 0.84%. The Baro-augmented ARAIM outperforms the baseline ARAIM for all $\sigma_{\text{int,Baro}} \leq 50$ m if $b_{\text{nom,Baro}} \leq 10$ m. The Baro augmentation even attains full coverage for $\sigma_{\text{int,Baro}} = 7.5$ m if $b_{\text{nom,Baro}} \leq 1$ m. However, all combinations with $b_{\text{nom,Baro}} \geq 15$ m have slightly poorer performance in comparison with the baseline. It can also be noted that increases in $b_{\text{nom,Baro}}$ or $\sigma_{\text{int,Baro}}$ have similar impacts on availability.

We ran 35 additional simulations to study the variation in LPV-200 availability coverage (with VAL = 35 or 20 m) with respect to single parameters of the error and threat models derived in Section 4. Figure 14 depicts the results of these simulations. For the results shown in the top row, we varied $\sigma_{\text{int,Baro}}$, with $\sigma_{\text{acc,Baro}}$ held at $\frac{2}{3}\sigma_{\text{int,Baro}}$. The center and bottom rows show the effect of variations in $b_{\text{nom,Baro}}$ and P_{Baro}, respectively. For each of the three sensitivity studies corresponding to these three parameters, the two other parameters were held constant at the empirical values defined in Section 4.

Figure 14 (top row) shows that the Baro-augmented ARAIM outperforms the baseline ARAIM, even for large values of $\sigma_{\text{int,Baro}}$ (and therefore of $\sigma_{\text{acc,Baro}}$). In particular, the Baro augmentation achieves higher coverage with VAL = 35 m, even for $\sigma_{\text{int,Baro}} = 150$ m. In contrast, in the case of VAL = 20 m, the improvement introduced by the Baro augmentation becomes negligible starting from $\sigma_{\text{int,Baro}} =$ 100 m. We note that, even for VAL = 20 m, 100% coverage can be reached with the empirical values of $b_{\text{nom,Baro}}$ and P_{Baro}. However, this would only be possible if the value of $\sigma_{\text{int,Baro}}$ could be reduced to 7.5 m.

The central row of Figure 14 shows that $b_{\text{nom,Baro}}$ must be kept below 25 or 15 m in order for the Baro augmentation to extend the coverage for VAL = 35 or 20 m, respectively. For VAL = 35 m, the baseline ARAIM actually outperforms the Baro ARAIM for $b_{\text{nom,Baro}} > 25$ m. Intuitively, higher $b_{\text{nom,Baro}}$ values indicate that the barometric geodetic altitude measurements are expected to be less accurate. Above a certain threshold, the algorithm perceives barometric geodetic altitude measurements as inaccurate to the extent at which they no longer produce any benefit for

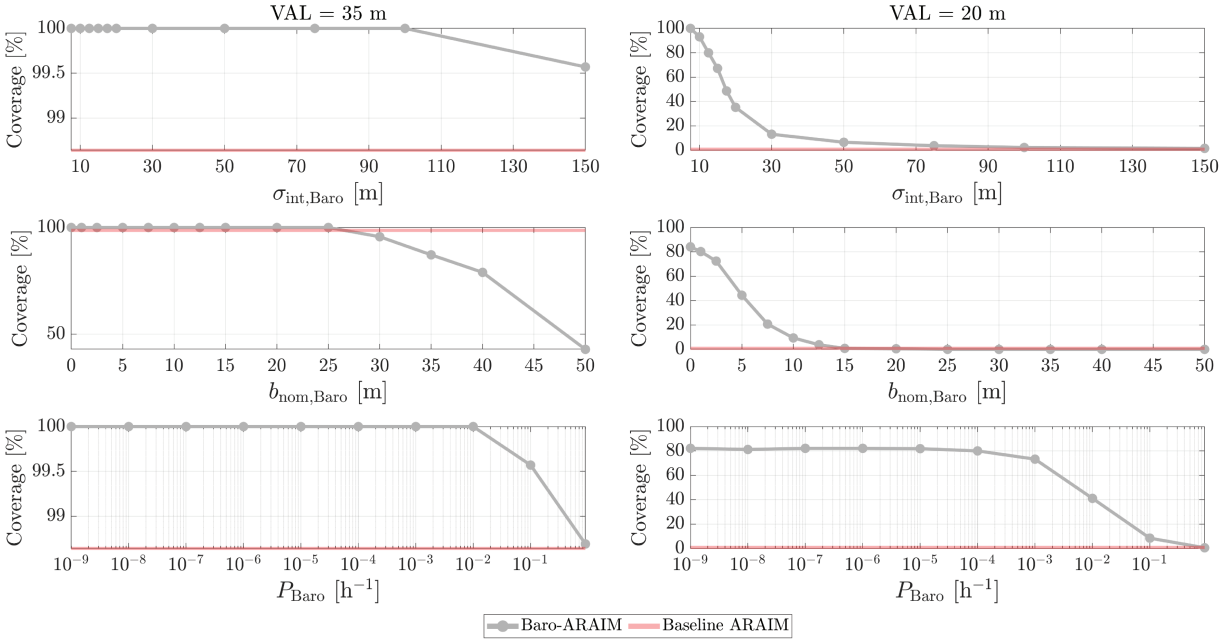

FIGURE 14 Global coverage of the 99.5 percentile of the LPV-200 availability for VAL = 35 m (left column) or VAL = 20 m (right column), as a function of $\sigma_{\text{int,Baro}}$ (top row), $b_{\text{nom,Baro}}$ (central row), or P_{Baro} (bottom row)

the navigation integrity. The combination of these measurements with GNSS measurements may actually worsen integrity, as shown in Figure 14. Mathematically, higher $b_{\text{nom,Baro}}$ values imply higher values of $b_q^{(k)}$ (see Appendix A). Conversely, higher $b_q^{(k)}$ values translate to higher HPL values (if q is 1 or 2) and higher VPL values (if q is 3). In turn, higher PLs may reduce the coverage of certain services, as in this case for the LPV-200 with VAL = 35 m. The reader is referred to the work by Blanch et al. (2015) for details of these mathematical relations.

The bottom row of Figure 14 shows that it is sufficient that $P_{\text{Baro}} < 0.9\ \text{h}^{-1}$ for the Baro-augmented ARAIM to outperform the baseline. Finally, it can be noted that, in the Baro-augmented ARAIM case, lowering P_{Baro} below 10^{-2} or 10^{-5} does not further increase the coverage with VAL = 35 or 20 m, respectively.

5.1.2 | *Availability Simulations with Empirical Error and Threat Models*

We ran an availability simulation of the Baro-augmented ARAIM with the empirical nominal and threat error models of Section 4. Figure 15 shows the results of

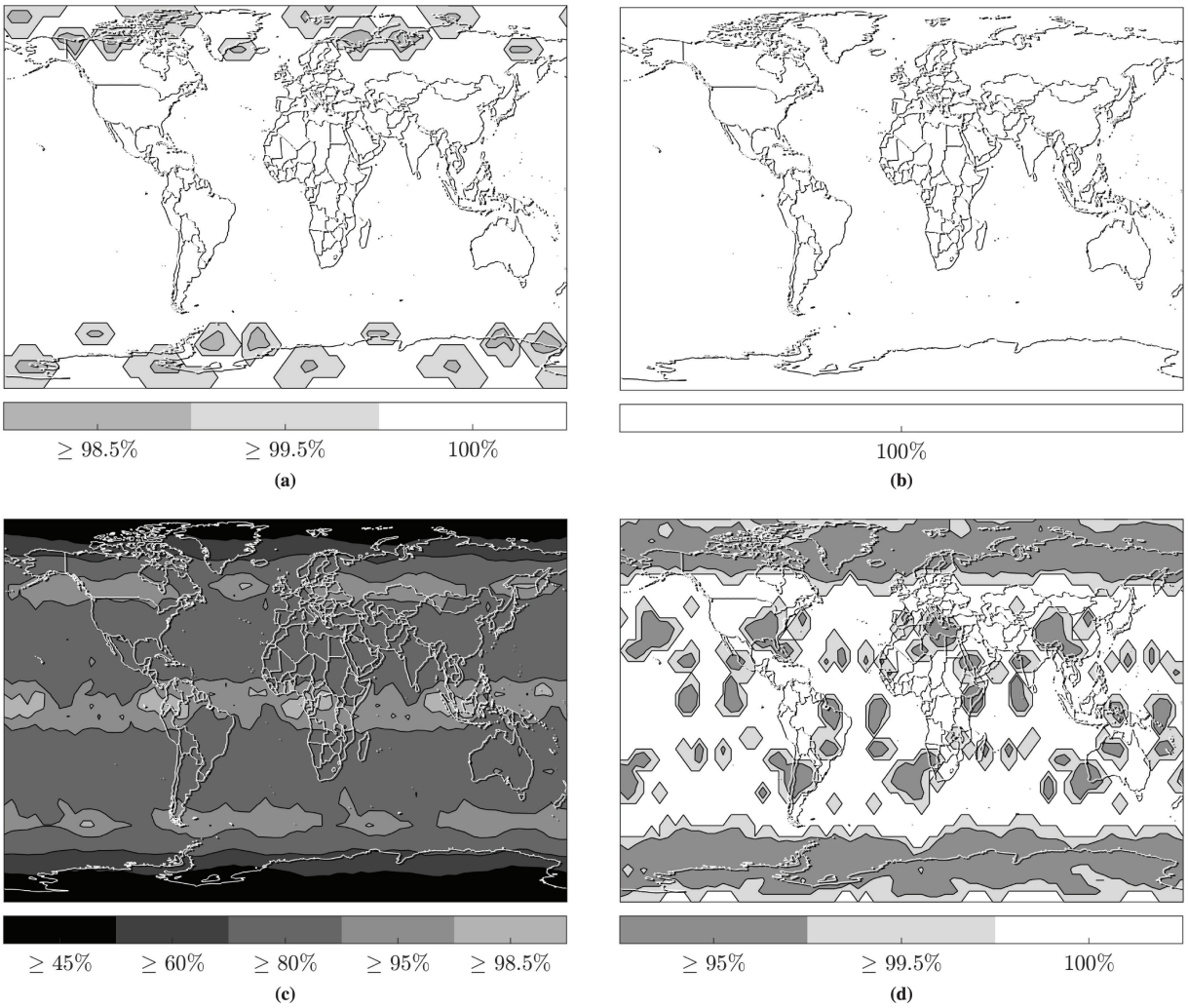

FIGURE 15 Availability with VAL = 35 m (top) or VAL = 20 m (bottom) achieved by baseline ARAIM (left) or Baro ARAIM (right) (a) Availability (VAL = 35 m) with baseline ARAIM (b) Availability (VAL = 35 m) with Baro ARAIM (c) Availability (VAL = 20 m) with baseline ARAIM (d) Availability (VAL = 20 m) with Baro ARAIM

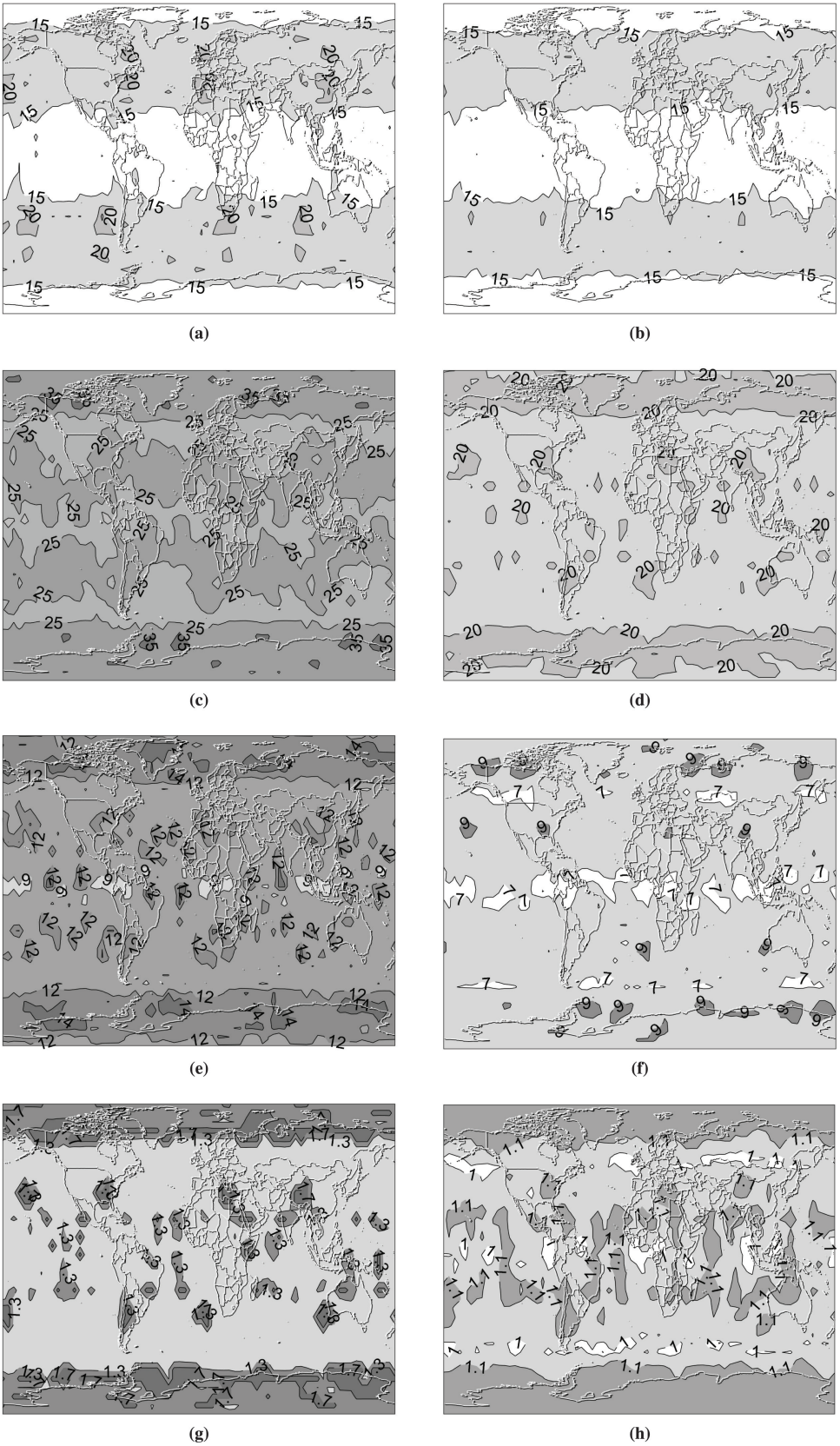

FIGURE 16 99.5 percentile of HPL (row 1), VPL (row 2), EMT (row 3), and $\sigma_{v,acc}$ (row 4) achieved by baseline ARAIM (left column) and Baro ARAIM (right column) (a) HPL achieved with baseline ARAIM (b) HPL achieved with Baro ARAIM (c) VPL achieved with baseline ARAIM (d) VPL achieved with Baro ARAIM (e) EMT achieved with baseline ARAIM (f) EMT achieved with Baro ARAIM (g) $\sigma_{v,acc}$ achieved with baseline ARAIM (h) $\sigma_{v,acc}$ achieved with Baro ARAIM

this simulation and of the corresponding baseline ARAIM simulation in terms of the achieved 99.5 percentile of the LPV-200 availability. Figure 16 shows the results in terms of PLs, EMT, and $\sigma_{v,acc}$.

The second row in Figure 16 shows that the Baro augmentation can significantly reduce the VPLs worldwide. Some improvements in HPL can be observed because of a better conditioning of the geometric matrices $\mathbf{H}^{(k)}$ and therefore of the estimator matrices $\mathbf{S}^{(k)}$, which are affected by the pseudo-inverse of $\mathbf{H}^{(k)}$ (Zampieri et al., 2020). Moreover, additional vertical information may also improve the performance in the horizontal domain by reducing the need to project pseudorange measurement information in the vertical domain. The lower half of Figure 16 shows that the Baro augmentation reduces the EMT and the standard deviation of the vertical position solution. Finally, comparing Figure 15 with Figure 16 shows that the availability of LPV-200 and of LPV-200 with VAL = 20 m is especially limited by the vertical navigation performance.

5.2 | Evaluation Along a Flight Trajectory

We evaluated the Baro-augmented ARAIM along the seventh of the nine flights shown in Figure 6. The three-dimensional (3D) trajectory of the aforementioned flight is shown in Figure 17, where the color shading from grey to black is proportional to the elapsed time since take-off. Figure 18 shows the evolution of the integrity-related performance indicators along the flight.

For the GNSS part of the system, we employed the same nominal biases and fault probabilities given in Table 4, whereas we set $\sigma_{URA} = 2.4$ m (representative of future GPS III civil navigation (CNAV) message ephemerides, according to Working Group C (2016)) and $\sigma_{URE} = 1.6$ m (i.e., $\sigma_{URA} \times 2/3$) for both GPS and Galileo. We considered these standard deviation values to be more realistic for the specific available GNSS measurements and for the time when the flight was carried out (July 2018). The values assigned to the additional constants and

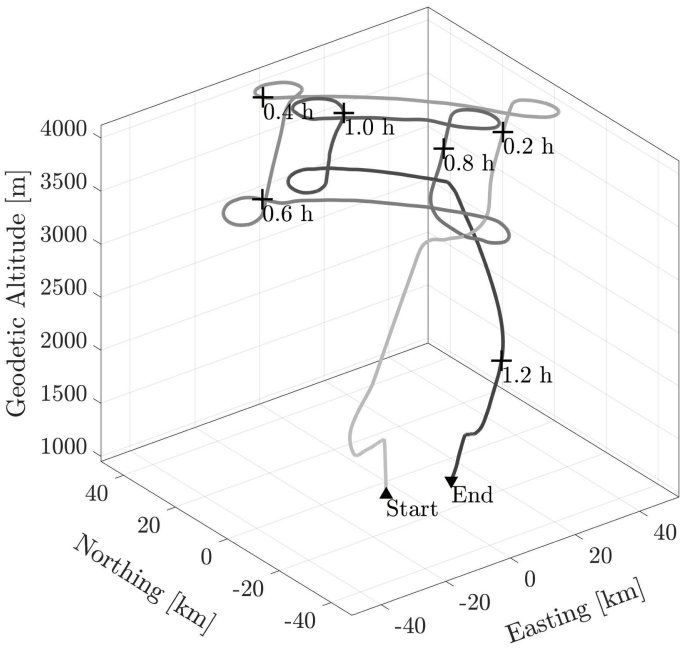

FIGURE 17 3D trajectory of the test flight used for evaluation of the Baro-augmented ARAIM

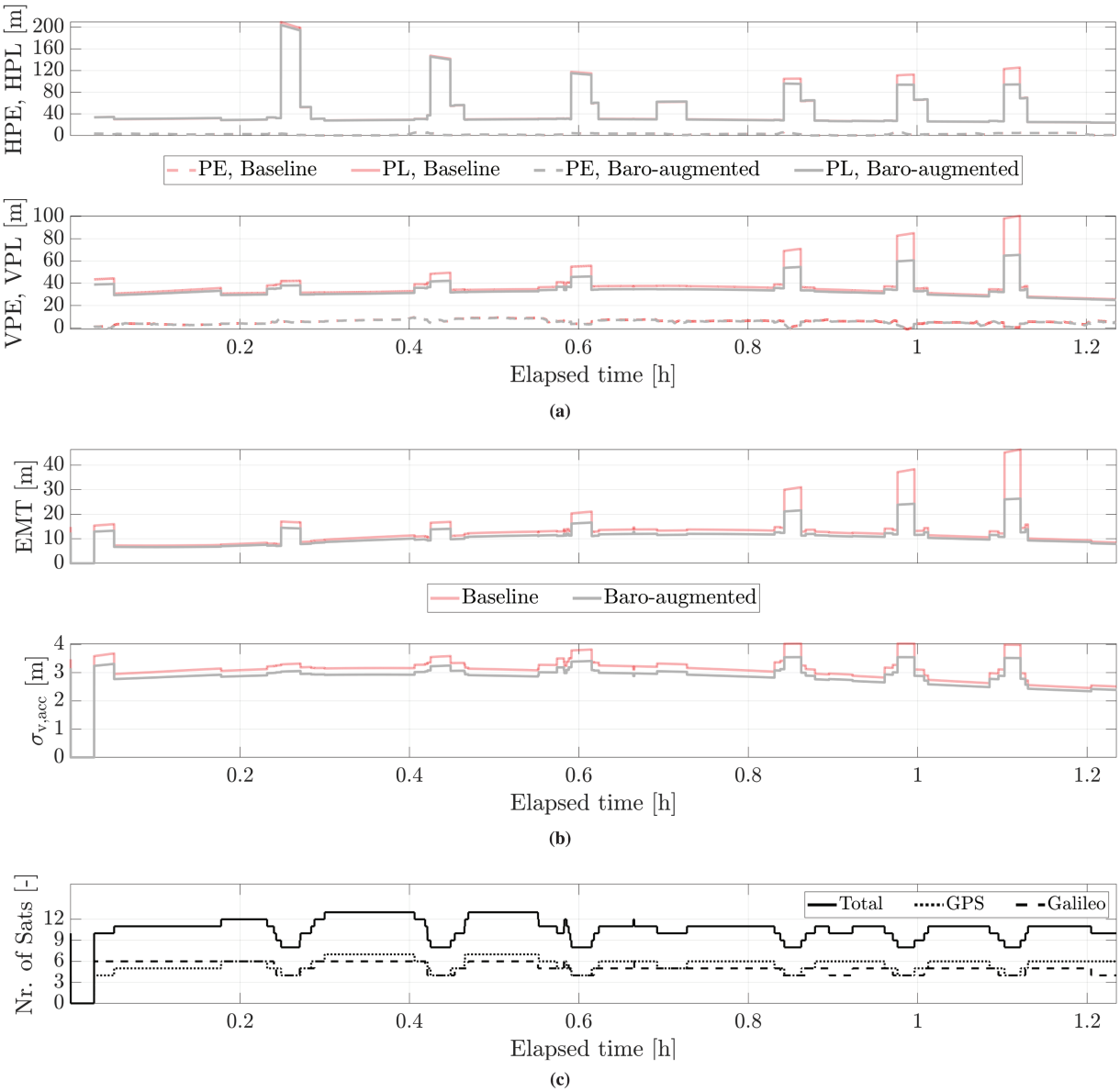

FIGURE 18 Results of applying the Baro-augmented ARAIM to a test flight (a) Positioning errors (PEs) and PLs (b) EMT and vertical standard deviation of the all-in-view solution, $\sigma_{v,acc}$ (c) Number of employed satellites

parameters mentioned in Appendix A correspond to those recommended by Working Group C (2016) for LPV-200.

As opposed to the availability simulations, the flight data evaluation captures the effect of aircraft maneuvers on the count of visible satellites, as shown in Figure 18(c). We note that the Galileo constellation was not complete at the time of the flights (July 2018), and few GPS satellites were transmitting at the L5 frequency. For this reason, in order to show a closer future performance of the proposed system, we have used L1/L2 GPS measurements for the real data evaluation for both the baseline ARAIM and Baro ARAIM implementations. In addition, we considered a cycle-slip detector, which reduced the availability of satellites in some cases, as smoothing filters require time to re-initialize.

The first row of Figure 18(a) shows the horizontal position error (HPE) and HPL achieved with the Baro-augmented and baseline ARAIM along the flight. From

this figure, it can be seen that the changes in HPE introduced by the Baro augmentation are almost negligible. The HPLs are approximately the same outside of those flight phases when sharper maneuvers were flown. During some of these phases, particularly during the last three phrases, the Baro augmentation is able to reduce the HPL by up to approximately 30 m. This reduction is possible because of the changes in the geometry matrix introduced by the inclusion of the barometric geodetic altitude measurements (see Section 5.1.2).

The second row in Figure 18(a) shows the vertical position error (VPE) and VPL achieved with the Baro-augmented and baseline ARAIM along the trajectory. As for the horizontal domain, the changes in the position error due to the Baro augmentation are found to be almost negligible. In contrast to the VPE results, the Baro-augmented ARAIM outperforms the baseline ARAIM in terms of the VPL along the whole flight. In particular, outside of the sharper maneuvers, the VPL is reduced by up to approximately 3 m. During the maneuvers, the reduction in VPL reaches almost 35 m.

In summary, the Baro-augmented ARAIM is able to reduce the PLs, particularly in cases of reduced reception of satellite measurements. The PLs do not decrease by the same amount during every aircraft banking maneuver. The reason for this is that the impact of barometric geodetic altitude measurements on the PLs depends on the specific geometry of the satellite–aircraft system, which changes from one epoch to another. Figure 18(b) shows that the developments of the EMT and the standard deviation of the vertical position solution are similar to those of the PLs.

6 | CONCLUSION

This paper presented a methodology for computing an accurate geodetic altitude, which we call the barometric geodetic altitude, from airborne barometric pressure measurements and external weather data. This paper then described the derivations of error and threat models of the barometric geodetic altitude computed with measurements collected during a DLR flight test campaign. Finally, this work adopted the derived empirical models for the augmentation of ARAIM with the barometric geodetic altitude (herein called Baro augmentation) and applied the resulting integrity architecture to worldwide availability simulations and to a real flight.

This work shows that the barometric geodetic altitude is remarkably closer to the true geodetic altitude than the QNE pressure altitude, if the latter is interpreted as the geodetic altitude. Moreover, it is found that the barometric geodetic altitude does not present altitude-dependent deviations from the true geodetic altitude, as opposed to the QNE pressure altitude. Residual altitude errors are found to exhibit a linear dependency on the aircraft pitch attitude angle, which allows for the derivation of a linear model to mitigate this impact. This approach leads to a further decrease in the absolute values of the mean and standard deviation of the error distribution down to 0.1 m and 4.1 m, respectively.

The simulations of the augmented GNSS ARAIM presented in this paper indicate that the Baro augmentation is capable of extending the full availability of the LPV-200 service worldwide when employing empirical error models. Even when the VAL is decreased from 35 to 20 m, the simulations show that the Baro-augmented ARAIM achieves a 79.75% world coverage of the 99.5 availability percentile, as opposed to the negligible coverage attained with the baseline ARAIM. Additionally, the simulations show that the tested architecture has the potential of achieving 100% coverage with this stricter requirement if tighter, hypothetical, nominal error

models are used. This finding motivates future efforts to derive tighter error models by analyzing data collected during many additional flights performed with different types of airplanes.

Implementing the Baro-augmented ARAIM along a real flight shows that this approach may have a marginal impact on the positioning accuracy in normal flight situations. Nonetheless, the Baro augmentation is found to have a non-negligible impact on the PLs, EMT, and $\sigma_{v,acc}$. A comparison of the PLs achieved with and without the Baro augmentation shows that the HPL and VPL are decreased by up to approximately 30 and 35 m, respectively, during aircraft banking maneuvers.

Ultimately, the proposed methodologies have the potential of supporting ATM or UAM applications requiring robust vertical navigation and of significantly improving ABAS performance, particularly during the final approach. Furthermore, this barometric geodetic altitude computation scheme and the empirical error models may be employed within stand-alone vertical navigation architectures or within integrated architectures featuring additional systems, such as APNT systems and/or INS.

To provide a general (and perhaps certifiable) error model and design, further investigations with additional flight or weather data will be performed in the future. The flights investigated in the current analysis covered a broad spectrum of altitudes, where measurements from certain altitudes were much less numerous than others. Furthermore, the flights portray only a small proportion of all possible scenarios, as they were performed in a short range of time, with low diversity in terms of regions covered and with a constant airplane–sensor combination. These are additional motivations for analyzing larger sets of flight and weather data to gain confidence in the derived models, to extend their applicability to different aircraft, and to account for yearly weather variability. The weather data employed is this work were obtained from the ECMWF ERA5 climate reanalysis on pressure levels. In the future, we intend to analyze the impact of different types of weather data on the weather-corrected pressure altitude computation. Furthermore, we aim to explore the use of weather forecasts rather than climate reanalysis to assess the described methodologies in a hypothetical real-time scenario.

ACKNOWLEDGMENTS

The flight data used for the analysis of this work were recorded during the flight campaign of the DLR project ALPS. We would like to thank all DLR colleagues involved in the coordination and execution of the flight trials. We would also like to thank the aeronautics program directorate of DLR for funding this research.

CONFLICT OF INTEREST

The authors declare no potential conflicts of interest.

REFERENCES

American Institute of Aeronautics and Astronautics. (2010). *Guide to reference and standard atmosphere models (AIAA G-003C-2010(2016))*. https://doi.org/10.2514/4.867842.001

Amin, H., Sjöberg, L. E., & Bagherbandi, M. (2019). A global vertical datum defined by the conventional geoid potential and the Earth ellipsoid parameters. *Journal of Geodesy*, *93*, 1943–1961. https://doi.org/10.1007/s00190-019-01293-3

Aviation Cooperation and Strategies Division. (2018). *UAS ATM CARS, Common altitude reference system.* European Organisation for the Safety of the Air Navigation (EUROCONTROL). Directorate of European Civil-Military Aviation (DECMA). https://www.eurocontrol.int/sites/default/files/2019-05/uas-atm-cars-v1.0-release-20181127_0.pdf

Blanch, J., Walter, T., & Enge, P. (2019). Gaussian bounds of sample distributions for integrity analysis. *IEEE Transactions on Aerospace and Electronic Systems*, *55*(4), 1806–1815. https://doi.org/10.1109/TAES.2018.2876583

Blanch, J., Walter, T., Enge, P., Lee, Y., Pervan, B., Rippl, M., Spletter, A., & Kropp, V. (2015). Baseline advanced RAIM user algorithm and possible improvements. *IEEE Transactions on Aerospace and Electronic Systems*, *51*(1), 713–732. https://doi.org/10.1109/TAES.2014.130739

Blanchard, R. L. (1971). A new algorithm for computing inertial altitude and vertical velocity. *IEEE Transactions on Aerospace and Electronic Systems*, *AES-7*(6), 1143–1146. https://doi.org/10.1109/TAES.1971.310216

Blanchard, R. L. (1972). An improvement to an algorithm for computing aircraft reference altitude. *IEEE Transactions on Aerospace and Electronic Systems*, *AES-8*(5), 685–687. https://doi.org/10.1109/TAES.1972.309586

Concept of Operations for European UTM Systems consortium. (2019). *U–space concept of operations.* Single European Sky ATM Research Programme Joint Undertaking. https://www.sesarju.eu/sites/default/files/documents/u-space/CORUS%20ConOps%20vol2.pdf

Di Vito, V., Torrano, G., Cerasuolo, G., & Ferrucci, M. (2021). Tactical separation system for small air transport vehicles: design advancements in the COAST project. *Proc. of the 10th EASN International Conference on Innovation in Aviation & Space to the Satisfaction of the European Citizens (10th EASN 2020), IOP Conference Series: Materials Science and Engineering*, 1024. https://doi.org/10.1088/1757-899X/1024/1/012085

European Center for Medium-Range Weather Forecasts. (2020). *Fact sheet: Reanalysis.* [Fact sheet]. https://www.ecmwf.int/en/about/media-centre/focus/2020/fact-sheet-reanalysis

Gaglione, S., Angrisano, A., Castaldo, G., Gioia, C., Innac, A., Perrotta, L., Del Core, G., & Troisi, S. (2015). GPS/barometer augmented navigation system: Integration and integrity monitoring. *Proc. of the 2015 IEEE Metrology for Aerospace (MetroAeroSpace),* Benevento, Italy, 166–171. https://doi.org/10.1109/MetroAeroSpace.2015.7180647

Garcia Crespillo, O. (2022). *GNSS/INS Kalman filter integrity monitoring with uncertain time correlated error processes* (Publication No. 7634) [Doctoral dissertation, EPFL Swiss Federal Institute of Technology in Lausanne]. Infoscience, EPFL Scientific Publications. https://doi.org/10.5075/epfl-thesis-7634

Giez, A., Mallaun, C., Zöger, M., Dörnbrack, A., & Schumann, U. (2017). Static pressure from aircraft trailing-cone measurements and numerical weather-prediction analysis. *Journal of Aircraft*, *54*(5), 1728–1737. https://doi.org/10.2514/1.C034084

Groves, P. D. (2013). *Principles of GNSS, inertial, and multisensor integrated navigation systems*. Artech House. https://uk.artechhouse.com/Principles-of-GNSS-Inertial-and-Multisensor-Integrated-Navigation-Systems-Second-Edition-P2033.aspx

Hersbach, H., Bell, B., Berrisford, P., Biavati, G., Horányi, A., Muñoz Sabater, J., Nicolas, J., Peubey, C., Radu, R., Rozum, I., Schepers, D., Simmons, A., Soci, C., Dee, D., & Thépaut, J.-N. (2023). *ERA5 hourly data on pressure levels from 1940 to present. Copernicus Climate Change Service (C3S) Climate Data Store (CDS).* https://doi.org/10.24381/cds.bd0915c6

International Civil Aviation Organization. (1993). *Manual of ICAO standard atmosphere, extended to 80 kilometres (262500 feet) (Doc 7488)* (3rd ed.). https://store.icao.int/en/manual-of-the-icao-standard-atmosphere-extended-to-80-kilometres-262500-feet-doc-7488

International Civil Aviation Organization. (2013). *Performance based navigation, (PBN) manual (Doc 9613)* (4th ed.). https://skybrary.aero/bookshelf/doc-9613-performance-based-navigation-manual-advance-4th-ed

International Civil Aviation Organization. (2016). *Procedures for air navigation services, Air traffic management (Doc 4444)* (16th ed.). https://store.icao.int/en/procedures-for-air-navigation-services-air-traffic-management-doc-4444

International Civil Aviation Organization. (2018a). *Annex 10 to the convention on international civil aviation, Aeronautical telecommunications, Volume I, Radio navigation aids* (7th ed.). https://ffac.ch/wp-content/uploads/2020/09/ICAO-Annex-10-Aeronautical-Telecommunications-Vol-I-Radio-Navigation-Aids.pdf

International Civil Aviation Organization. (2018b). *Annex 3 to the convention on international civil aviation, Meteorological service for international air navigation* (20th ed.). https://store.icao.int/en/annex-3-meteorological-service-for-international-air-navigation

International Civil Aviation Organization. (2018c). *Procedures for air navigation services, Aircraft operations, Volume I – Flight procedures (Doc 8168)* (6th ed.). https://store.icao.int/en/procedures-for-air-navigation-services-pans-aircraft-operations-volume-i-flight-procedures-doc-8168

International Civil Aviation Organization. (2018d). *Procedures for air navigation services, Aircraft operations, Volume III - Aircraft operating procedures (Doc 8168)* (1st ed.). https://store.icao.int/en/procedures-for-air-navigation-services-pans-aircraft-operations-volume-iii-aircraft-operating-procedures-doc-8168

International Organization for Standardization. (1975). *Standard atmosphere* (ISO Standard No. 2533:1975). https://www.iso.org/standard/7472.html

Jan, S., Gebre-Egziabher, D., Walter, T., & Enge, P. (2008). Improving GPS-based landing system performance using an empirical barometric altimeter confidence bound. *IEEE Transactions on Aerospace and Electronic Systems*, *44*(1), 127–146. https://doi.org/10.1109/TAES.2008.4516994

Lee, J., Hyeon, E., Kim, M., & Lee, J. (2016). Vertical position error bounding for integrated GPS/barometer sensors to support unmanned aerial vehicle (UAV). *Proc. of the 30th Congress of the International Council of the Aeronautical Sciences (ICAS),* Daejeon, Korea. https://www.icas.org/ICAS_ARCHIVE/ICAS2016/data/preview/2016_0295.htm

Lemoine, F. G., Kenyon, S. C., Factor, J. K., Trimmer, R. G., Pavlis, N. K., Chinn, D. S., Cox, C. M., Klosko, S. M., Luthcke, S. B., Torrence, M. H., Wang, Y. M., Williamson, R. G., Pavlis, E. C., Rapp, R. H., & Olson, T. R. (1998). *The development of the joint NASA GSFC and the National Imagery and Mapping Agency (NIMA) geopotential model EGM96.* https://ntrs.nasa.gov/citations/19980218814

Lerro, A., & Battipede, M. (2021). Safety analysis of a certifiable air data system based on synthetic sensors for flow angle estimation. *Applied Sciences*, *11*(7), 3127. https://doi.org/10.3390/app11073127

Li, T.-C., & Chueh, V. (2010). Errors in the pressure and Blanchard altitudes for a cross country flight. *Proc. of the IEEE/ION Position, Location, and Navigation Symposium (PLANS 2010)*, Indian Wells, CA, 1295–1303. https://doi.org/10.1109/PLANS.2010.5507348

Nossek, E., Suess, M., Belabbas, B., & Meurer, M. (2014). Analysis of position and timing solutions for an APNT-system– A look on convergence, accuracy and integrity. *Proc. of the 27th International Technical Meeting of the Satellite Division of the Institute of Navigation (ION GNSS+ 2014)*, Tampa, FL, 3040–3047. https://www.ion.org/publications/abstract.cfm?articleID=12295

Osechas, O., Fohlmeister, F., Dautermann, T., & Felux, M. (2022). Impact of GNSS–band radio interference on operational avionics. *NAVIGATION*, *69*(2). https://doi.org/10.33012/navi.516

Osechas, O., Narayanan, S., Garcia Crespillo, O., Zampieri, G., Battista, G., Kumar, R., Schneckenburger, N., Lay, E., Belabbas, B., & Meurer, M. (2019). Feasibility demonstration of terrestrial RNP with LDACS. *Proc. of the 32nd International Technical Meeting of the Satellite Division of the Institute of Navigation (ION GNSS+ 2019)*, Miami, FL, 3254–3265. https://doi.org/10.33012/2019.17119

Piwek, K., & Wiśniowski, W. (2016). Small air transport aircraft entry requirements evoked by FlightPath 2050. *Aircraft Engineering and Aerospace Technology*, *88*(2), 341–347. https://doi.org/10.1108/AEAT-02-2015-0065

Quanterion Solutions Incorporated. (2016). *Quanterion nonelectronic parts reliability data–2016*. Reliability Databook Series, Quanterion Solutions Incorporated. https://www.quanterion.com/product/publications/nonelectronic-parts-reliability-datapublication-nprd-2016/

Radio Technical Commission for Aeronautics. (2020). *Minimum operational performance standards (MOPS) for GNSS aided inertial systems, DO-384.* https://my.rtca.org/productdetails?id=a1B1R00000LowzIUAR

Reid, T., Walter, T., Blanch, J., & Enge, P. (2016). GNSS integrity in the arctic. *NAVIGATION*, *63*(4), 469–492. https://doi.org/10.1002/navi.169

Scherllin-Pirscher, B., Steiner, A. K., Kirchengast, G., Schwärz, M., & Leroy, S. S. (2017). The power of vertical geolocation of atmospheric profiles from GNSS radio occultation. *Journal of Geophysical Research: Atmospheres*, *122*(3), 1595–1616. https://doi.org/10.1002/2016JD025902

Shively, C. A., & Hsiao, T. T. (2005). Error and availability analysis of category IIIb LAAS augmented by radar altimeter. *NAVIGATION*, *52*(3), 155–162. https://doi.org/10.1002/j.2161-4296.2005.tb01742.x

Single European Sky ATM Research Programme Joint Undertaking. (2020). *ICARUS concept definition: State-of-the-art, requirements, gap analysis.* https://www.u-spaceicarus.eu/wp-content/uploads/2022/07/D3.1_ICARUS_CONCEPT_DEFINITION.pdf

Single European Sky ATM Research Programme Joint Undertaking. (2021). *ICARUS preliminary CONOPS.* https://www.u-spaceicarus.eu/wp-content/uploads/2022/07/SESAR-2020-ER-ICARUS-D4.3_ICARUS_Preliminary-CONOPS.pdf

Single European Sky ATM Research Programme Joint Undertaking. (2022). *ICARUS–integrated common altitude reference system for U–space.* https://www.u-spaceicarus.eu

Siouris, G. M. (1993). *Aerospace avionics systems: A modern synthesis.* Academic Press.

Torens, C., Volkert, A., Becker, D., Gerbeth, D., Schalk, L., Garcia Crespillo, O., Zhu, C., Stelkens-Kobsch, T., Gehrke, T., Metz, I. C., & Dauer, J. (2021). HorizonUAM: Safety and security considerations for urban air mobility. *Proc. of the AIAA AVIATION 2021 FORUM*. https://doi.org/10.2514/6.2021-3199

Videmsek, A., Uijt de Haag, M., & Bleakley, T. (2019). Radar altimeter aiding of GNSS for precision approach and landing of RPA. *Proc. of the 2019 Integrated Communications, Navigation and Surveillance Conference (ICNS 2019),* Herndon, VA. 1–16. https://doi.org/10.1109/ICNSURV.2019.8735258

Walter, T., & Blanch, J. (2019). *MAAST.* https://gps.stanford.edu/resources/software-tools/maast

Walter, T., Blanch, J., Gunning, K., Joerger, M., & Pervan, B. (2019). Determination of fault probabilities for ARAIM. *IEEE Transactions on Aerospace and Electronic Systems*, *55*(6), 3505–3516. https://doi.org/10.1109/TAES.2019.2909727

Working Group C. (2016). *Working Group C - ARAIM technical subgroup, Milestone 3 report.* https://www.gps.gov/policy/cooperation/europe/2016/working-group-c/

World Geodetic System and Geomatics Focus Group. (2014). *Department of Defense World Geodetic System 1984, Its definition and relationships with local geodetic systems.* National Center for Geospatial Intelligence Standards (NCGIS), National Geospatial-Intelligence Agency (NGA). https://nsgreg.nga.mil/doc/view?i=4085

Xu, X., Lai, J., Liu, M., Zheng, Z., Dai, Y., & Huang, K. (2021). An improved weight optimization AAIM method aided by barometric altimeter. *International Journal of Aeronautical and Space Sciences*, *22*(3), 638–647. https://doi.org/10.1007/s42405-020-00321-3

Zampieri, G., Narayanan, S., Crespillo, O. G., & Osechas, O. (2020). A regularized least squares estimator for pseudorange-based terrestrial positioning under degraded geometries. *Proc. of the 33rd International Technical Meeting of the Satellite Division of the Institute of Navigation (ION GNSS+ 2020)*, 698–707. https://doi.org/10.33012/2020.17690

How to cite this article: Simonetti, M., & García Crespillo, O. (2024). Geodetic altitude from barometer and weather data for GNSS integrity monitoring in aviation. *NAVIGATION, 71*(2). https://doi.org/10.33012/navi.637

APPENDIX

A | MAIN ASPECTS OF THE GNSS WLS AND BASELINE ARAIM ALGORITHMS

This appendix summarizes the main aspects of the baseline ARAIM algorithm that are relevant for this paper. For further details, the reader is referred to the works by Working Group C (2016) and Blanch et al. (2015).

At each epoch, all of the considered Galileo and GPS satellite measurements are employed to produce a navigation solution $\mathbf{x}$, which consists of the receiver position and receiver clock biases. The position and clock unknowns are typically computed via linearization of the pseudorange observation equation and with iterations based on the following WLS estimator:

$$\Delta\hat{\mathbf{x}} = \mathbf{S}\Delta\mathbf{z} = \left(\left[\mathbf{H}^T\mathbf{W}\mathbf{H}\right]\right)^{-1}\mathbf{H}^T\mathbf{W}\Delta\mathbf{z} \tag{A1}$$

where $\Delta\mathbf{z}$ is $\Delta\boldsymbol{\rho} = \boldsymbol{\rho} - \hat{\boldsymbol{\rho}}$. The vector $\boldsymbol{\rho}$ contains pseudorange measurements after dual-frequency and tropospheric corrections and smoothing. The vector $\hat{\boldsymbol{\rho}}$ consists of expected ranging values based on estimated satellites and user positions and is corrected for the estimated receiver clock biases. The geometry matrix $\mathbf{H}$ is as follows:

$$\mathbf{H} = \begin{pmatrix} \mathbf{u}_{\text{Gal}}^{1} & 1 & 0 \\ \vdots & \vdots & \vdots \\ \mathbf{u}_{\text{Gal}}^{n_{\text{Gal}}} & 1 & 0 \\ \mathbf{u}_{\text{GPS}}^{1} & 0 & 1 \\ \vdots & \vdots & \vdots \\ \mathbf{u}_{\text{GPS}}^{n_{\text{GPS}}} & 0 & 1 \end{pmatrix} \tag{A2}$$

where n_{Gal} and n_{GPS} are the number of available Galileo and GPS pseudorange measurements, respectively. The vector $\mathbf{u}^i$ denotes the line of sight vector in the

ENU frame from the user to the i-th satellite. The weight matrix $\mathbf{W}$ of the estimator is the inverse of the measurement covariance matrix $\mathbf{\Sigma}$ used for integrity:

$$\mathbf{\Sigma} = \mathrm{diag}\left(\left[\begin{array}{cccccc} \sigma^2_{\mathrm{int,Gal},1} & \cdots & \sigma^2_{\mathrm{int,Gal},n_{\mathrm{Gal}}} & \sigma^2_{\mathrm{int,GPS},1} & \cdots & \sigma^2_{\mathrm{int,GPS},n_{\mathrm{GPS}}} \end{array}\right]\right)$$
$$\text{with} \quad \sigma^2_{\mathrm{int,Gal},i} = \sigma^2_{\mathrm{URA,Gal},i} + \sigma^2_{\mathrm{Gal},i} \quad \text{and} \quad \sigma^2_{\mathrm{int,GPS},i} = \sigma^2_{\mathrm{URA,GPS},i} + \sigma^2_{\mathrm{GPS},i}$$

where $\sigma_{\mathrm{URA},i}$ denotes the i-th satellite's standard deviation of the clock and ephemeris error used for integrity. The second parameter σ_i is an additional term for residual tropospheric and user-side errors (typically noise and multipath).

ARAIM is based on an MHSS algorithm. The GNSS faults that must be monitored are determined from the probabilities of the single-satellite faults, $P_{\mathrm{sat,Gal}}$ or $P_{\mathrm{sat,GPS}}$, and of the constellation-wide faults, $P_{\mathrm{const,Gal}}$ or $P_{\mathrm{const,GPS}}$.

First, the algorithm computes the maximum number of concurrent faults that must be monitored, denoted as $N_{\mathrm{fault,max}}$ and defined as follows:

$$N_{\mathrm{fault,\,max}} = \max\left\{ r \in \left\{1, \ldots, N_{\mathrm{meas}}\right\} \middle| P_{\mathrm{multiple}}\left(r+1, P_{\mathrm{event},1}, \ldots, P_{\mathrm{event},N_{\mathrm{meas}}+N_{\mathrm{const}}}\right) \le P_{\mathrm{thres}} \right\} \tag{A3}$$

where $N_{\mathrm{meas}} = n_{\mathrm{Gal}} + n_{\mathrm{GPS}}$ and N_{const} denotes the number of available GNSS constellations, which can be 0, 1, or 2, as only GPS and Galileo are considered. The term P_{thres} is the chosen threshold for the integrity risk coming from unmonitored faults. The function $P_{\mathrm{multiple}}\left(r, P_{\mathrm{event},1}, \ldots, P_{\mathrm{event},N_{\mathrm{meas}}} + N_{\mathrm{cons}}\right)$ denotes the probability of all of the fault modes consisting of at least r independent events, with the following:

$$P_{\mathrm{event},i} = P_{\mathrm{sat},i} \quad \text{and} \quad P_{\mathrm{event},N_{\mathrm{meas}}+j} = P_{\mathrm{const},j} \quad \text{with} \quad i \in \left\{1, \ldots, N_{\mathrm{meas}}\right\} \quad \text{and} \quad j \in \left\{1, \ldots, N_{\mathrm{const}}\right\} \tag{A4}$$

Secondly, all of the N_{subsets} possible combinations of $N_{\mathrm{fault,max}}$ or fewer events are determined. All of the satellite subsets that correspond to these combinations are then generated. The algorithm forms N_{subsets} satellite subsets, where the k-th subset contains all of the satellites that are fault-free in the k-th combination, with $k \in \left\{1, \ldots, N_{\mathrm{subsets}}\right\}$. Subsequently, the ARAIM algorithm computes from each k-th subset its corresponding k-th navigation solution, which is obtained from the measurements of all satellites in the k-th subset. The navigation solutions computed with these satellite subsets are known as fault-free solutions and are denoted with $\mathbf{x}^{(k)}$.

Based on a comparison of the *all-in-view* and fault-free solutions within a *solution separation* test, it is possible to determine whether a certain fault mode is present. In the case of no fault detection, it is possible to compute the HPL and VPL. The error and threat models are necessary to build the solution separation tests and to compute the PLs. The parameters defining these models are expected to be obtained from a broadcast integrity support message, as listed below:

- the nominal bias used for integrity, $b_{\mathrm{nom,Gal}}$ or $b_{\mathrm{nom,GPS}}$,
- the standard deviation of the clock and ephemeris errors used for integrity, $\sigma_{\mathrm{URA,Gal}}$ or $\sigma_{\mathrm{URA,GPS}}$,

- the standard deviation of the clock and ephemeris error used for accuracy and continuity, $\sigma_{\mathrm{URE,Gal}}$ or $\sigma_{\mathrm{URE,GPS}}$, and
- the probability of satellite and constellation-wide faults, $P_{\mathrm{sat,Gal}}$ and $P_{\mathrm{const,Gal}}$ or $P_{\mathrm{sat,GPS}}$ and $P_{\mathrm{const,GPS}}$.

The standard deviations σ_{URA} and nominal biases b_{nom} are elements of the GNSS nominal error models for integrity, whereas the standard deviations for accuracy and continuity σ_{URE} are part of the GNSS nominal error models for accuracy and continuity. The PLs are computed based on the following implicit equation:

$$2Q\left(\frac{\mathrm{PL_q}-b_q^{(0)}}{\sigma_q^{(0)}}\right)+\sum_{k=1}^{N_{\mathrm{subsets}}}P_{\mathrm{fault},k}\,Q\left(\frac{\mathrm{PL_q}-T_{k,q}-b_q^{(k)}}{\sigma_q^{(k)}}\right)=P_{\mathrm{HMI,mon,q}}\quad\text{with } q\in\{1,2,3\}\tag{A5}$$

where $P_{\mathrm{fault},k}$ is the prior probability of the k-th fault mode. The quantities $T_{k,q}$, $b_q^{(k)}$, and $\sigma_q^{(k)}$ are the solution separation threshold in the dimension q, the nominal bias projected into the dimension q, and the variance of the navigation solution in the dimension q, respectively, of the k-th subset. The superscript 0 refers to subset number 0, which corresponds to the all-in-view set of satellites. The dimensions 1, 2, and 3 correspond to the east, north, and up spatial components, respectively. Depending on the dimension q, the term $\mathrm{PL_q}$ represents the HPL along the east or north axis or the VPL, which are denoted by $\mathrm{HPL_E}$, $\mathrm{HPL_N}$, and VPL, respectively. The overall HPL is the square root of the sum of the squares of $\mathrm{HPL_E}$ and $\mathrm{HPL_N}$. The term $P_{\mathrm{HMI,mon,q}}$ corresponds to the probability of a fault that may result in hazardously misleading information in the dimension q and that needs to be monitored. Finally, $Q(\cdot)$ is the tail probability function of a normal distribution with zero mean and unit variance.

The ARAIM algorithm requires the definition of further constants and design parameters that are related to integrity, such as P_{thres}, as well as others related to accuracy and continuity. Their description is beyond the scope of this paper, as the Baro augmentation has no influence on these parameters. The values defined for the LPV-200 service are used by Walter & Blanch (2019) or prescribed or recommended by Working Group C (2016).